

FABRICATION OF SnO₂ LAYER AS ELECTRON
TRANSPORT LAYERS FOR PEROVSKITE SOLAR CELLS



Miss Rattanaphon Thanimkan

จุฬาลงกรณ์มหาวิทยาลัย
CHULALONGKORN UNIVERSITY

A Thesis Submitted in Partial Fulfillment of the Requirements
for the Degree of Master of Science in Physics
Department of Physics
FACULTY OF SCIENCE
Chulalongkorn University
Academic Year 2020
Copyright of Chulalongkorn University

การประดิษฐ์ชั้นดีบุกออกไซด์เป็นชั้นการส่งผ่านอิเล็กตรอนสำหรับเซลล์สุริยะเพอรอฟสไกต์



วิทยานิพนธ์นี้เป็นส่วนหนึ่งของการศึกษาตามหลักสูตรปริญญาวิทยาศาสตรมหาบัณฑิต

สาขาวิชาฟิสิกส์ ภาควิชาฟิสิกส์

คณะวิทยาศาสตร์ จุฬาลงกรณ์มหาวิทยาลัย

ปีการศึกษา 2563

ลิขสิทธิ์ของจุฬาลงกรณ์มหาวิทยาลัย

Thesis Title FABRICATION OF SnO₂ LAYER AS ELECTRON
TRANSPORT LAYERS FOR PEROVSKITE SOLAR
CELLS
By Miss Rattanaphon Thanimkan
Field of Study Physics
Thesis Advisor Assistant Professor SOJIPHONG CHATRAPHORN,
Ph.D.

Accepted by the FACULTY OF SCIENCE, Chulalongkorn University in
Partial Fulfillment of the Requirement for the Master of Science

..... Dean of the FACULTY OF
SCIENCE
(Professor POLKIT SANGVANICH, Ph.D.)

THESIS COMMITTEE

..... Chairman
(Associate Professor THITI BOVORN RATANARAKS,
Ph.D.)

..... Thesis Advisor
(Assistant Professor SOJIPHONG CHATRAPHORN,
Ph.D.)

..... Examiner
(Associate Professor SOMCHAI KIATGAMOLCHAI,
Ph.D.)

..... External Examiner
(Associate Professor RACHSAK SAKDANUPHAB, Ph.D.)

จุฬาลงกรณ์มหาวิทยาลัย
CHULALONGKORN UNIVERSITY

รัตนภรณ์ ถนิมกาญจน์ : การประดิษฐ์ชั้นดีบุกออกไซด์เป็นชั้นการส่งผ่านอิเล็กตรอนสำหรับ
เซลล์สุริยะเพอโรฟสไกต์. (FABRICATION OF SnO₂ LAYER AS
ELECTRON TRANSPORT LAYERS FOR PEROVSKITE
SOLAR CELLS) อ.ที่ปรึกษาหลัก : ผศ. ดร. โสจิพงษ์ ถัตราภรณ์

ชั้นการส่งผ่านอิเล็กตรอนของดีบุกออกไซด์ (SnO₂) ได้รับความสนใจเป็นอย่างมากสำหรับเซลล์สุริยะเพอโรฟสไกต์ เนื่องจากชั้นดีบุกออกไซด์มีข้อดีหลากหลาย เช่น มีช่องว่างระหว่างแถบพลังงานที่กว้าง, ความเสถียรภาพทางแสงและทางเคมีที่ดี, ความโปร่งใสสูง, การเคลื่อนที่ของอิเล็กตรอนสูงและการจัดเตรียมได้ง่าย ในงานวิจัยชิ้นนี้ชั้นดีบุกออกไซด์ถูกประดิษฐ์โดยวิธีการเคลือบแบบหมุนเหวี่ยงและวิธีอาร์เอพแมกเนตรอนสปีดเตอริงโดยการเปลี่ยนเงื่อนไขต่างๆ ชั้นดีบุกออกไซด์ถูกรวบรวมอยู่ในโครงสร้างแนวระนาบของเซลล์สุริยะเพอโรฟสไกต์ซึ่งประกอบด้วย FTO/SnO₂/MAPbI₃/spiro-OMeTAD/Au สำหรับการเคลือบแบบหมุนเหวี่ยง พบว่าฟิล์มดีบุกออกไซด์สามารถเคลือบทั่วแผ่นของ FTO แต่ฟิล์มดีบุกออกไซด์มีอนุภาคบางส่วนของสารตั้งต้นดีบุกออกไซด์ ซึ่งสังเกตได้จากภาพถ่ายของกล้องจุลทรรศน์อิเล็กตรอนแบบส่องกราด สำหรับวิธีอาร์เอพแมกเนตรอนสปีดเตอริง พบว่าพื้นผิวของฟิล์มดีบุกออกไซด์บนกระจกโซดาไลม์มีผิวเรียบ ค่าการส่งผ่านของแสงอยู่ในช่วงระหว่าง 85 - 90% ในช่วงความยาวคลื่นที่ตามองเห็น และพบว่าค่าความหนาที่เหมาะสมอยู่ในช่วงระหว่าง 35 - 40 นาโนเมตร ค่าความกว้างของช่องว่างระหว่างแถบพลังงานของดีบุกออกไซด์ที่จัดเตรียมโดยวิธีสปีดเตอริงมีค่าประมาณ 4.2 eV เซลล์สุริยะที่ใช้ดีบุกออกไซด์โดยวิธีสปีดเตอริงมีประสิทธิภาพและเสถียรภาพที่สูงกว่าเซลล์สุริยะที่ใช้ดีบุกออกไซด์โดยวิธีการเคลือบแบบหมุนเหวี่ยงจึงควรหลีกเลี่ยงกระบวนการทางเคมีที่ใช้สารละลายเพื่อลดจำนวนอนุภาคจากการตกผลึกของสารตั้งต้นดีบุกออกไซด์ ซึ่งทำให้พื้นผิวของชั้นส่งผ่านอิเล็กตรอนไม่เรียบ พบว่าเซลล์สุริยะเพอโรฟสไกต์ที่ใช้ดีบุกออกไซด์โดยวิธีสปีดเตอริง ซึ่งใช้พาวเวอร์สปีดเตอริง 60 วัตต์ และความดันแก๊สอาร์กอน (Ar) 1×10^{-3} มิลลิบาร์ ที่ความดันแก๊สออกซิเจน (O₂) 1×10^{-4} มิลลิบาร์ ให้ประสิทธิภาพสูงสุดประมาณ 17.7%.

สาขาวิชา ฟิสิกส์

ลายมือชื่อนิติ

ปีการศึกษา 2563

ลายมือชื่อ อ.ที่ปรึกษาหลัก

6172046523 : MAJOR PHYSICS

KEYWORD: PEROVSKITE SOLAR CELLS, ELECTRON TRANSPORT LAYER,
TIN OXIDE

Rattanaphon Thanimkan : FABRICATION OF SnO₂ LAYER AS ELECTRON
TRANSPORT LAYERS FOR PEROVSKITE SOLAR CELLS . Advisor: Asst.
Prof. SOJIPHONG CHATRAPHORN, Ph.D.

A SnO₂ has attracted more attention as electron transport layer (ETL) for perovskite solar cells (PSCs) because it has diverse advantages, e.g., wide bandgap energy, excellent optical and chemical stability, high transparency, high electron mobility, and easy preparation. In this work, SnO₂ layer was fabricated by spin-coating and RF magnetron sputtering techniques with various conditions. The SnO₂ layer was integrated into the planar structure of PSCs consisting of FTO/SnO₂/MAPbI₃/spiro-OMeTAD/Au. For spin-coating, SnO₂ films can fully cover the FTO, but it has some particulates from recrystallization of SnO₂ precursor as observed in the FESEM images. For RF sputtering technique, morphology of SnO₂ films on SLG substrates is very smooth. The optical transmission of the SnO₂ films was approximately 85 - 90% in the visible region. It was found that the optimum thickness of SnO₂ layer was approximately 35 - 40 nm. The band gap energy (E_g) of SnO₂ by sputtering was about 4.2 eV. The sputtered SnO₂ based devices were demonstrated to have better device performance and stability than spin-coated SnO₂ based devices. Wet chemical processes were avoided to minimize the particulates from recrystallization of SnO₂ precursor that led to uneven surface of the ETL layer. It was found that the PSC based on sputtered SnO₂, with the sputtering power of 60 W and Ar gas pressure of 1×10^{-3} mbar with O₂ gas partial pressure of 1×10^{-4} mbar delivered champion power conversion efficiency (PCE) of about 17.7%.



Field of Study: Physics
Academic Year: 2020

Student's Signature
Advisor's Signature

ACKNOWLEDGEMENTS

I would like to express my sincere thanks to my thesis advisor, Assistant Professor Dr. Sojiphong Chatraphorn for helping throughout the course of this research. I am most grateful for teaching and advice, not only the research methodologies but also many other methodologies in life.

I would like to give thanks for suggestion from the chairman and the committee: Associate Professor Dr. Thiti Bovornratanaraks, Associate Professor Dr. Somchai Kiatgamolchai and Associate Professor Dr. Rachsak Sakdanuphab.

I would like to thank all the member of the Semiconductor Physics Research Laboratory (SPRL): Miss Kwanruthai Butsriruk and Mr. Passakorn Phiromruk for their kind help, friendliness and encouragement throughout the period of this research. I would also like to thank Dr. Boonyaluk Namnuam for helping with the sputtering techniques and surface profiler measurements. In addition, I would also like to thank Mr. Pornsak Panchawirat for helping with the FESEM and EDS measurements.

Finally, I most gratefully acknowledge my parents and my partners: Mr. Aisarapap Supasuk for all their support throughout my study. I would not have achieved this far and this thesis would not have been completed without all the support that I have always received from them.

TABLE OF CONTENTS

	Page
ABSTRACT (THAI)	iii
ABSTRACT (ENGLISH).....	iv
ACKNOWLEDGEMENTS	v
TABLE OF CONTENTS.....	vi
LIST OF FIGURES	ix
LIST OF TABLES	xiii
CHAPTER I INTRODUCTION	14
1.1 Overview	14
1.2 Objectives.....	18
1.3 Thesis outline	19
CHAPTER II PEROVSKITE SOLAR CELLS FABRICATION METHODS AND CHARACTERIZATION TECHNIQUES	20
2.1 Perovskite solar cells (PSCs) structure	20
2.2 Deposition techniques.....	23
2.2.1 Spin-coating method.....	23
2.2.2 RF magnetron sputtering techniques	23
2.3 Material characterization techniques	24
2.3.1 Field-Emission Scanning Electron Microscopy (FESEM)	24
2.3.2 Atomic Force Microscopy (AFM).....	25
2.3.3 Optical Transmission Spectroscopy.....	26
2.3.4 Surface profiler	29
2.3.5 Current density-voltage (J-V) measurement	30
CHAPTER III FABRICATION AND CHARACTERIZATION OF THE SnO ₂ AND PEROVSKITE SOLAR CELLS	31
3.1 Perovskite solar cells fabrication.....	31
3.1.1 Substrate preparation	31

3.1.2 Fabrication of SnO ₂ films.....	32
3.1.2.1 SnO ₂ films by spin-coating method	32
3.1.2.2 SnO ₂ films by RF magnetron sputtering technique.....	33
3.1.3 Fabrication of TiO ₂ films	34
3.1.3.1 TiO ₂ compact layer (cp-TiO ₂).....	34
3.1.3.2 TiO ₂ mesoporous layer (mp-TiO ₂).....	34
3.1.4 Fabrication of perovskite absorber layer.....	35
3.1.5 Fabrication of hole transport layer.....	36
3.1.6 Fabrication of Au metal electrode	36
3.2 Characterizations	37
3.2.1 Field-Emission Scanning Electron Microscopy (FESEM)	37
3.2.2 Atomic Force Microscopy (AFM).....	38
3.2.3 Optical Transmission Spectroscopy.....	38
3.2.4 Surface profiler	38
3.2.5 Current density-voltage (J-V) measurement	38
CHAPTER IV RESULTS AND DISCUSSION.....	39
4.1 Characteristics of spin-coated SnO ₂ films.....	39
4.1.1 The surface morphology of spin-coated SnO ₂ films.....	39
4.1.2 The optical transmission spectrum of spin-coated SnO ₂ films	51
4.2 Characteristics of sputtered SnO ₂ films	52
4.2.1 The surface morphology of sputtered SnO ₂ films	52
4.2.2 The optical transmission spectrum of sputtered SnO ₂ films	54
4.3 Properties of perovskite solar cells (PSCs)	55
4.3.1 Characteristics of perovskite absorber layers.....	55
4.3.2 J-V characteristics of spin-coated SnO ₂ films as ETLs	58
4.3.3 J-V characteristics of sputtered SnO ₂ films as ETLs.....	61
4.3.4 J-V characteristics of TiO ₂ films as ETLs.....	65
CHAPTER V CONCLUSTION.....	67
REFERENCES.....	69

VITA..... 73



จุฬาลงกรณ์มหาวิทยาลัย
CHULALONGKORN UNIVERSITY

LIST OF FIGURES

	Page
Figure 1 Schematic diagram of ABX ₃ perovskite structure [8].	14
Figure 2 Schematic diagrams showing configuration of solar cells: (a) dye sensitized solar cells (DSSCs) and (b) perovskite solar cells (PSCs) [9].	15
Figure 3 Morphologies of SnO ₂ as ETL deposited by different methods; (a) SnO ₂ films deposited on FTO substrate by ALD method and (b) SnO ₂ layers deposited on FTO substrate by spin-coating and CBD method [22].	16
Figure 4 The relationship between electrical resistivity of SnO ₂ films and oxygen partial pressure percentage [26].	18
Figure 5 Schematic diagrams showing (a) normal planar structure and (b) energy band diagram and charge transfer process of PSC [27].	20
Figure 6 Schematic diagrams of generic structures; (a) normal (n-i-p) planar, (b) inverted (p-i-n) planar, and (c) mesoporous (conventional) structure of PSCs [29]. ..	22
Figure 7 Schematic illustration of magnetron sputtering system [32].	24
Figure 8 Schematic illustration of field-emission scanning electron microscopy (FESEM) [33].	25
Figure 9 Schematic illustration of an atomic force microscope (AFM) [34].	26
Figure 10 Schematic diagram showing optical paths of the UV-Vis-NIR spectrophotometer (Shimadzu Model UVPC1600).	27
Figure 11 Schematic diagram of optical transmission and reflection in the thin film.	28
Figure 12 Photograph of measurement result by Dektak ³ ST surface profiler.	29
Figure 13 Schematic diagram of the normal planar structure of PSCs.	31
Figure 14 Schematic diagrams of preparation with FTO substrate for transparent electrode.	32
Figure 15 Schematic diagrams of preparation with SnO ₂ films for ETL.	32
Figure 16 Schematic diagrams showing spin-coating method of SnO ₂ films.	33
Figure 17 Schematic diagram showing the RF magnetron sputtering deposition process. Ar and O ₂ gas were used during sputtering process.	33
Figure 18 Schematic diagrams of preparation with cp-TiO ₂ layers for ETLs.	34
Figure 19 Schematic diagrams of preparation with mp-TiO ₂ layers for ETLs.	35

Figure 20 Schematic diagrams of two-step spin-coating method to deposit MAPbI ₃ perovskite films.	35
Figure 21 Photograph of the N ₂ -filled glovebox (Changsha Tianchuang Powder Technology Co., Ltd.).....	36
Figure 22 Photograph of a shadow mask for Au metal electrode.	37
Figure 23 Schematic diagrams of preparation with SnO ₂ films for thickness measurement by Dektak ³ ST surface profiler.	38
Figure 24 (a) FESEM image and (b) EDS spectrum of SLG substrate.	40
Figure 25 (a) FESEM image and (b) EDS spectrum of spin-coated SnO ₂ film on SLG substrate without particle in the SnO ₂ surface.	41
Figure 26 (a) FESEM image and (b) EDS spectrum of spin-coated SnO ₂ film on SLG substrate with particle in the SnO ₂ surface.	42
Figure 27 FESEM images of spin-coated SnO ₂ film on SLG substrates using SnCl ₄ .5H ₂ O dissolved in IPA with varying precursor concentration (a) 0.1 M and (b) 0.2 M while keeping spin speed at 3000 rpm for 40 s and annealing on a hotplate at 250 °C for 30 min.	43
Figure 28 FESEM images of spin-coated SnO ₂ film on SLG substrates using SnCl ₂ .2H ₂ O dissolved in ethanol with varying precursor concentration (a) 0.05 M, (b) 0.1 M, (c) 0.2 M, (d) 0.25 M, (e) 0.3 M, and (f) 0.5 M while keeping spin speed at 3000 rpm for 40 s and annealing on a hotplate at 200 °C for 60 min.	44
Figure 29 FESEM images of spin-coated SnO ₂ film on SLG substrates using SnCl ₂ .2H ₂ O dissolved in ethanol (preheat solution) with varying precursor concentration (a) 0.1 M, (b) 0.3 M, (c) 0.5 M, and (d) 0.7 M while keeping spin speed at 3000 rpm for 40 s and annealing on a hotplate at 200 °C for 60 min.....	45
Figure 30 Optical transmission spectrum of spin-coated SnO ₂ film on SLG substrates using SnCl ₄ .5H ₂ O dissolved in IPA with varying precursor concentration while keeping spin speed at 3000 rpm for 40 s and annealing on a hotplate at 200 °C for 60 min.	51
Figure 31 Optical transmission spectrum of spin-coated SnO ₂ film on SLG substrates using SnCl ₂ .2H ₂ O dissolved in ethanol with varying precursor concentration while keeping spin speed at 3000 rpm for 40 s and annealing on a hotplate at 200 °C for 60 min.	52

Figure 32 FESEM image shows smooth surface morphology of sputtered SnO ₂ film on SLG substrate.	53
Figure 33 AFM images of 60 W RF sputtering power with (a) 40 nm and (b) 80 nm thickness of SnO ₂ films on SLG substrates.....	53
Figure 34 AFM image of 90 W RF sputtering power with 35 nm thickness of SnO ₂ films on SLG substrate.	54
Figure 35 Optical transmission spectrum of the sputtered SnO ₂ film on SLG substrates.....	55
Figure 36 FESEM image of surface morphology of perovskite absorber layers by two-step spin-coating method.	56
Figure 37 FESEM image of cross-section of perovskite absorber layers on FTO substrates.....	56
Figure 38 Optical transmission spectrum of perovskite absorber layers by two-step spin-coating method.	57
Figure 39 Tauc plot of perovskite absorber layers by two-step spin-coating method.....	57
Figure 40 FESEM image of cross-section of a complete PSCs with SnO ₂ by spin-coating method.	58
Figure 41 J-V curves of PSCs based on spin-coated SnO ₂ films with different spin speed; SnCl ₄ .5H ₂ O dissolved in IPA (0.15 M), annealing temperature at 200 °C for 60 min in air.	59
Figure 42 J-V curves of PSCs based on spin-coated SnO ₂ films with different SnCl ₄ .5H ₂ O solution concentration; SnCl ₄ .5H ₂ O dissolved in IPA, spin speed of 3000 rpm for 40 s, and annealing temperature at 200 °C for 60 min in air.....	60
Figure 43 Photograph of a complete PSCs with SnO ₂ by RF sputtering techniques.	61
Figure 44 FESEM image of cross-section of a complete PSCs with SnO ₂ by RF sputtering techniques.	61
Figure 45 J-V curves of PSCs based on sputtered SnO ₂ film with different deposition time; RF sputtering power of 60 W and Ar gas pressure of 1×10^{-3} mbar with O ₂ gas partial pressure of 1.5×10^{-4} mbar.	63
Figure 46 J-V curves of PSCs based on sputtered SnO ₂ film with different RF sputtering power; Ar gas pressure of 1×10^{-3} mbar with O ₂ gas partial pressure of 1.5×10^{-4} mbar.....	64

Figure 47 J-V curves of PSCs based on sputtered SnO ₂ film with different Ar gas pressures; RF sputtering power of 60 W and O ₂ gas partial pressure of 1.5×10^{-4} mbar.	64
Figure 48 J-V curves of the champion devices based on spin-coated cp-TiO ₂ / mp-TiO ₂ and sputtered SnO ₂ films of PSCs.....	66



LIST OF TABLES

	Page
Table 1 FESEM images of spin-coated SnO ₂ film on SLG substrates using SnCl ₄ .5H ₂ O dissolved in ethanol with annealing on a hotplate at 200 °C for 60 min.	46
Table 2 FESEM images of spin-coated SnO ₂ film on SLG substrates using SnCl ₄ .5H ₂ O dissolved in IPA with annealing on a hotplate at 250 °C for 30 min.	47
Table 3 FESEM images of spin-coated SnO ₂ film on SLG substrates using SnCl ₂ .2H ₂ O dissolved in ethanol with annealing on a hotplate at 200 °C for 60 min.	48
Table 4 FESEM images of spin-coated SnO ₂ film on SLG substrates using SnCl ₂ .2H ₂ O dissolved in IPA with annealing on a hotplate at 250 °C for 30 min.	50
Table 5 Photovoltaic parameters of PSCs with spin-coated SnO ₂ films as ETLs with different spin speed and SnCl ₄ .5H ₂ O solution concentration.	60
Table 6 The thicknesses of SnO ₂ films with different deposition time.	63
Table 7 Photovoltaic parameters of PSCs with sputtered SnO ₂ films as ETLs.....	65
Table 8 Photovoltaic parameters of the champion PSCs based on spin-coated cp-TiO ₂ / mp-TiO ₂ and sputtered SnO ₂ films.	66

CHAPTER I

INTRODUCTION

1.1 Overview

Due to increase of energy demand in daily activities in livelihood, which the available energy is mostly from the combustion of fossil fuel. Thus, the research and development in alternative sources of renewable energy may be necessary. These alternative sources include hydropower, nuclear power, wave and tidal power, solar cells, etc. A solar cell or photovoltaic device converts energy from the sunlight into electrical energy. There are several technologies to fabricated solar cells, such as copper indium gallium selenide solar cells (CIGS) [1], cadmium telluride solar cells (CdTe) [2], silicon solar cells (Si-SCs) [3], dye sensitized solar cells (DSSCs) [4], quantum dot solar cells (QDSCs) [5], organic photovoltaic cells (OPVs) [6], and perovskite solar cells (PSCs) [7].

A perovskite material has a chemical formula of ABX_3 with cubic crystal structure. For organic-inorganic halide perovskite, A is an organic cation, such as methylammonium ($CH_3NH_3^+$, MA^+) or formamidinium ($NH_2CHNH_2^+$, FA^+), B is a metal cation, such as Pb^{2+} or Sn^{2+} , and X is a halide anion, such as Cl^- , Br^- , I^- or mixed halide [8] as shown in Figure 1.

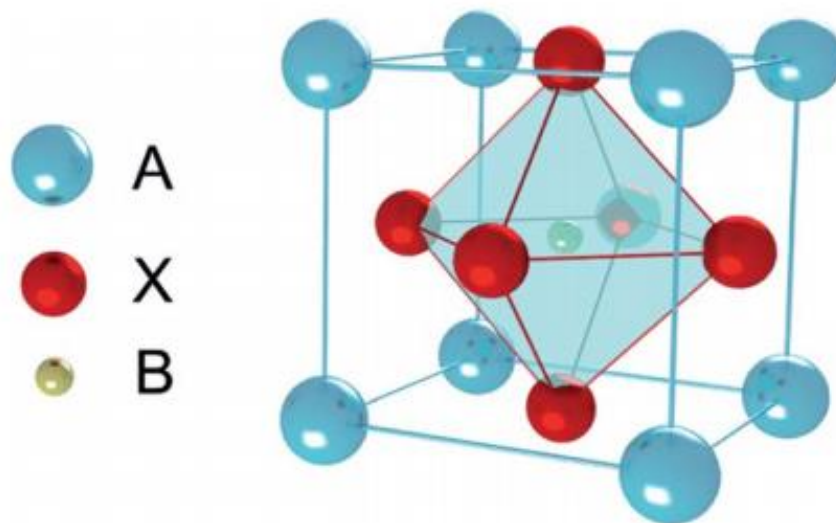


Figure 1 Schematic diagram of ABX_3 perovskite structure [8].

The structure of DSSCs consists of a transparent conductive oxide (TCO), such as fluorine-doped tin oxide (FTO) or indium-doped tin oxide (ITO), a nanocrystalline TiO_2 mesoporous film, Dye molecules, a redox liquid electrolyte, such as I^-/I_3^- dissolved in a solvent, and a counter electrode, such as a platinum (Pt) [9] as shown in Figure 2 (a). The increase internal surface area in the liquid electrolyte results in the increase of recombination processes, which charge transfer reactions occur between the electrons and the oxidized species (I_3^-) [10]. This problem was solved in DSSCs by the replacement of the liquid electrolyte into hole transport layer (HTL), such as Spiro-OMeTAD and using perovskite materials as absorbers, e.g. methylammonium lead iodide (MAPbI_3 or $\text{CH}_3\text{NH}_3\text{PbI}_3$) as shown in Figure 2 (b). This device has power conversion efficiency (PCE) as high as 27.4% [11].

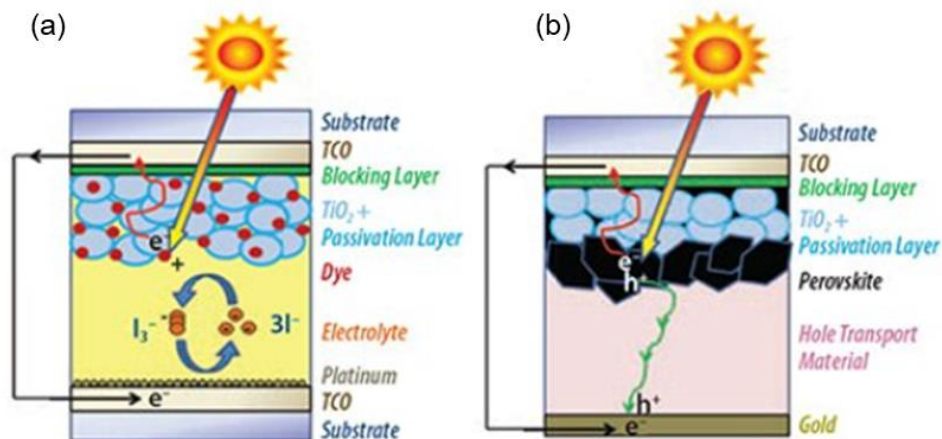


Figure 2 Schematic diagrams showing configuration of solar cells: (a) dye sensitized solar cells (DSSCs) and (b) perovskite solar cells (PSCs) [9].

The normal structure of PSCs consists of five layers, i.e., transparent electrode such as FTO or ITO, electron transport layer (ETL), perovskite absorber layer, hole transport layer (HTL), and metal electrode [12, 13]. The ETLs that have been proposed for PSCs are, for example, TiO_2 , ZnO , SnO_2 , etc. TiO_2 is usually used for ETL as a compact layer and a mesoporous layer. Both layers give relatively higher efficiency PSCs. However, TiO_2 layer has some limitations for PSCs, such as it needs high temperature process and yields low electron mobility. The effect of TiO_2 layer negatively affects the device stability under ultraviolet (UV) illumination [14, 15]. In

addition, ZnO is another choice of ETL. It can be deposited easily with low temperature process. However, ZnO is environmentally unstable due to the hydroxide (OH) residue on the ZnO surface causing the decomposition of perovskite layers [16]. Recently, SnO₂ has attracted interests as an ETL for PSCs because it has diverse advantages, e.g., wide bandgap energy (3.6 - 4.0 eV), excellent optical and chemical stability, high transparency, high electron mobility ($\sim 240 \text{ cm}^2/\text{Vs}$), and easy preparation [17].

There are several methods to deposit SnO₂ film as ETL for PSCs, such as spin-coating [18], magnetron sputtering [19], atomic layer deposition (ALD) [20], and chemical bath deposition (CBD) [21] as shown in Figure 3. Qi *et al.* reviewed the progresses in efficient and stable PSCs using SnO₂ as ETLs. SnO₂ showed a good band alignment with perovskite absorption, high transparency, and high electron mobility. The results suggest that SnO₂ is a wonderful ETL for PSCs [22].

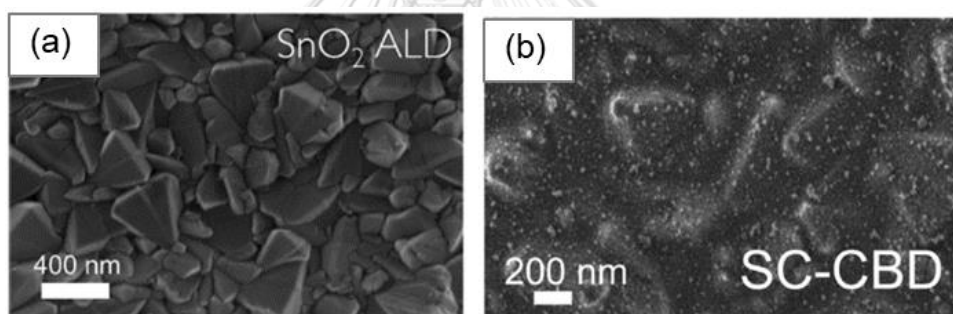


Figure 3 Morphologies of SnO₂ as ETL deposited by different methods; (a) SnO₂ films deposited on FTO substrate by ALD method and (b) SnO₂ layers deposited on FTO substrate by spin-coating and CBD method [22].

Kwang-Ho *et al.* [23] prepared SnO₂ ETL by spin-coating method using SnCl₄.5H₂O dissolved in IPA. The annealing temperature was varied from 100 °C to 500 °C and the concentration was investigated from 0.05 M to 0.2 M. The PSCs that were obtained with the thickness of 40 nm, precursor concentration of 0.1 M, and annealing temperature of 250 °C of SnO₂ film delivered a PCE of 19.17%.

Matthew *et al.* [24] fabricated SnO₂ by RF magnetron sputtering and spin-coating method. For RF magnetron sputtering, the SnO₂ film was deposited using SnO₂ target with 2 inch diameter. The SnO₂ target was sputtered in Ar (99.99%) and O₂

(99.99%) gas at a working pressure 0.25 Pa with sputtering power of 60 W. They varied the SnO₂ thickness for 20 nm, 40 nm, 60 nm, and 80 nm. For spin-coating method, the SnO₂ film was deposited using SnCl₂.2H₂O dissolved in ethanol (0.1 M). The SnO₂ film was spin-coated at 3000 rpm for 30 s and then annealed on a hotplate at 180 °C for 60 min in air. They found that the sputtered SnO₂ ETL demonstrated uniform and stability layer than spin-coated SnO₂ ETL based devices. The devices with 40 nm thickness of sputtered SnO₂ film showed the best performance with a PCE of 12.82%.

Guangfeng *et al.* [25] compared SnO₂ deposition processes between RF and DC magnetron sputtering; RF sputtering using nonconductive white SnO₂ target and DC sputtering using conductive gray SnO₂ target. They studied the effect of SnO₂ films on PSCs with varying Ar/O₂ ratios (1:1, 1:2, 2:1, and 2:3). The SnO₂ films fabricated by RF magnetron sputtering exhibited higher efficiency than DC magnetron sputtering. The device with Ar/O₂ ratio 2:3 showed a PCE of 17.43%.

Den *et al.* [26] used RF magnetron sputtering on SnO₂ ceramic disc target with 5N purity and 64 mm in diameter with the distance between target and substrate of 6 cm. The working pressure was 1 Pa in pure Ar and O₂ gas and sputtering power of 150 W. They studied the oxygen partial pressure percentage that was varied from 1% to 10%. They found that the increase in oxygen partial pressure results in the decrease of film thickness and the resistivity of SnO₂ film decreases with the increase of oxygen partial pressure as shown in Figure 4.

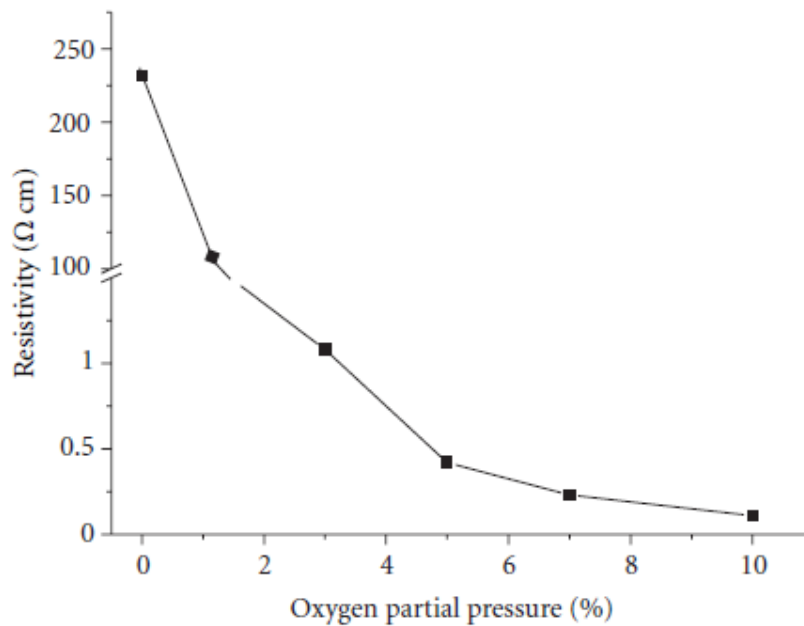


Figure 4 The relationship between electrical resistivity of SnO₂ films and oxygen partial pressure percentage [26].

In this work, we demonstrated normal planar structure of PSCs with optimized room-temperature-processed SnO₂ as ETL prepared by spin-coating and RF magnetron sputtering process. The MAPbI₃ perovskite thin film was deposited by two-step spin-coating method. The HTL was deposited using Spiro-OMeTAD solution by a spin-coating. The Au metal electrode was deposited on the HTL by the thermal evaporation. Two types of process were investigated and found that the devices based on SnO₂ film by RF magnetron sputtering showed superior performance. We considered the effects of RF sputtering parameters, such as deposition time, RF sputtering power, Ar gas pressure in the performance of the PSCs.

1.2 Objectives

- To fabricate SnO₂ layer as electron transport layers for normal structure of the perovskite solar cells.
- To study physical and optical properties of SnO₂ layer for the perovskite solar cells.
- To compare the performance of perovskite solar cells using SnO₂ and TiO₂ electron transport layers.

1.3 Thesis outline

The thesis consists of five chapters. The detailed backgrounds and the structure of PSCs, deposition techniques, and characterization techniques are introduced in Chapter II. The experimental details and characterizations are described in Chapter III. The results are discussed in Chapter IV. The last chapter is the conclusion.



CHAPTER II

PEROVSKITE SOLAR CELLS FABRICATION METHODS AND CHARACTERIZATION TECHNIQUES

This chapter describes material properties of perovskite solar cells (PSCs) and thin film deposition techniques, e.g., spin-coating and RF magnetron sputtering techniques. The characterization techniques, such as field-emission scanning electron microscopy (FESEM), atomic force microscopy (AFM), optical transmission spectroscopy, surface profiler, and current density-voltage (J-V) measurement are described.

2.1 Perovskite solar cells (PSCs) structure

The normal (n-i-p) planar structure of PSCs consists of five layers, i.e., transparent electrode (FTO), electron transport layer (ETL), perovskite absorber layer, hole transport layer (HTL), and metal electrode as shown in Figure 5 (a). The energy band diagram and the charge transfer process of PSCs showing the separation and collection of electrons and holes is shown in Figure 5 (b). The charge transfer process of device can be described. Firstly, perovskite absorber generates and separates electrons and holes when photons are incident on the absorber. Then, electrons and holes are transferred to the ETL and HTL, respectively. Finally, electrons move from the ETL to the FTO and holes move from the HTL to the metal electrode [27].

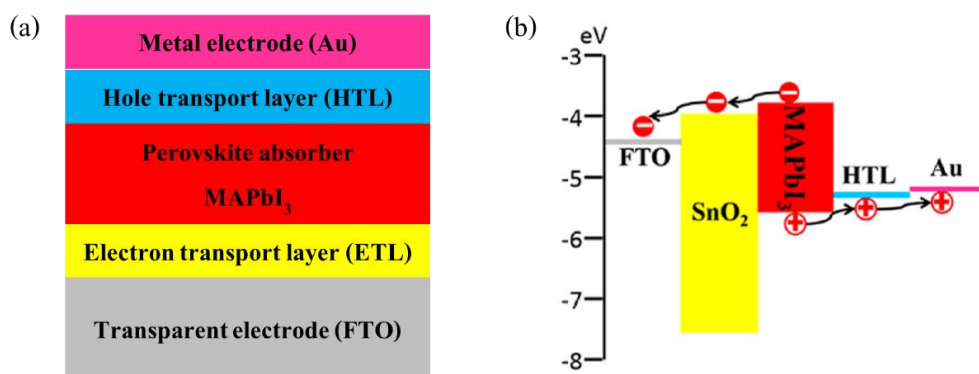


Figure 5 Schematic diagrams showing (a) normal planar structure and (b) energy band diagram and charge transfer process of PSC [27].

The material properties of perovskite solar cells (PSCs) are briefly described as follows;

(i) Transparent electrode

The transparent electrode on substrate is a critical component for PSCs. It should have high transmission, good conductivity, and promote good adhesion for the deposited layers. Fluorine-doped tin oxide (FTO) has attracted great attentions for transparent electrode because it is high transparency, chemically inert, and high temperature resistant.

(ii) Electron transport layer (ETL)

The ETL is the electron selective contact with perovskite absorber layer to extract electrons from perovskite absorber and also to prevent hole from moving to the transparent electrode. The requirements of ETL for high efficiency PSCs are (i) appropriate energy band alignment, (ii) high electron mobility, (iii) high optical transmittance, and (iv) high stability and easy processing. The ETLs that have been proposed for PSCs are, for example, TiO₂, ZnO, SnO₂, etc. At present, TiO₂ is usually used for ETL as a compact layer and a mesoporous scaffold layer (Figure 6 (c)). Both layers give relatively higher efficiency PSCs but it needs high temperature process and has low electron mobility (10^{-5} cm²/Vs), on the order below 1 cm²/Vs. On the other hand, SnO₂ has attracted interest as an ETL for PSCs because it has diverse advantages, e.g., wide bandgap energy about 3.6 - 4.0 eV, excellent optical and chemical stability, high transparency of 90% on glass, high electron mobility about 240 cm²/Vs, and easy preparation at low temperature process [28].

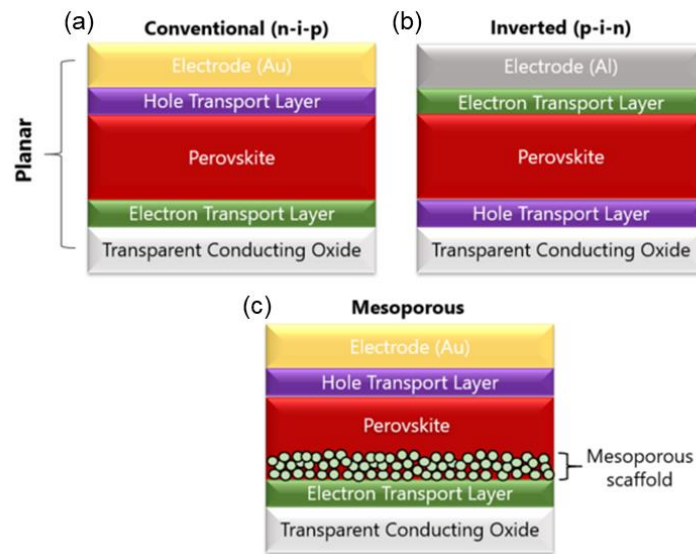


Figure 6 Schematic diagrams of generic structures; (a) normal (n-i-p) planar, (b) inverted (p-i-n) planar, and (c) mesoporous (conventional) structure of PSCs [29].

(iii) Perovskite absorber layer

The perovskite absorber layer absorbs photons to produce electrons and holes. MAPbI_3 is commonly used in the normal planar structure of PSCs (Figure 6 (a)), while it owns high absorption coefficients in the order of 10^5 cm^{-1} , high open-circuit voltage (V_{oc}), the carrier diffusion length of 100 nm and the bandgap of 1.55 eV [30].

(iv) Hole transport layer (HTL)

The HTL is used to collect and transport holes from perovskite absorber. The requirements of HTL for high efficiency PSCs are high hole mobility, acceptable energy levels that match with the perovskite absorber, and high stability and easy processing. The organic spiro-OMeTAD is usually used for HTL with the conductivity of about 10^{-5} S/cm and hole mobility of about $2 \times 10^{-4} \text{ cm}^2/\text{Vs}$ [31].

(v) Metal electrode

Gold (Au) is commonly used as electrode because it can preserve the stability of PSCs. The Au metal electrode is generally deposited by thermal evaporation technique.

2.2 Deposition techniques

In this work, the SnO₂ as ETL was fabricated by spin-coating and RF magnetron sputtering techniques which can be briefly described as follows.

2.2.1 Spin-coating method

Spin coating technique is one of techniques used to deposit thin films. For this process, liquid solution is deposited onto a substrate and then rotated at high speed. The rotation of a substrate at high speed and the centripetal force together with surface tension will cause the solution to spread and coat the substrate. The solvent is evaporated to leave of the substrate by annealing process. The thickness (t) of spin-coated film depends on the spin speed:

$$t \propto \frac{1}{\sqrt{\omega}} \quad (1)$$

where ω is the angular velocity.

2.2.2 RF magnetron sputtering techniques

Radio frequency (RF) magnetron sputtering is feasible to produce high quality film. The RF sputtering is usually used for oxide or insulating thin films. This process utilizes a strong magnetic field and electric field to ionize gas atoms (Ar⁺) in the vacuum chamber. The ions are accelerated to bombard the target. The momentum is transferred from the ions onto the target. At the same time, the atoms of the target are then emitted from the target to the substrate. The film quality depends on the sputtering gas pressure that affects the mean free path in the sputtering process. However, in the film fabrication process, the sputtering power affects the film morphology, structure and performance of devices.

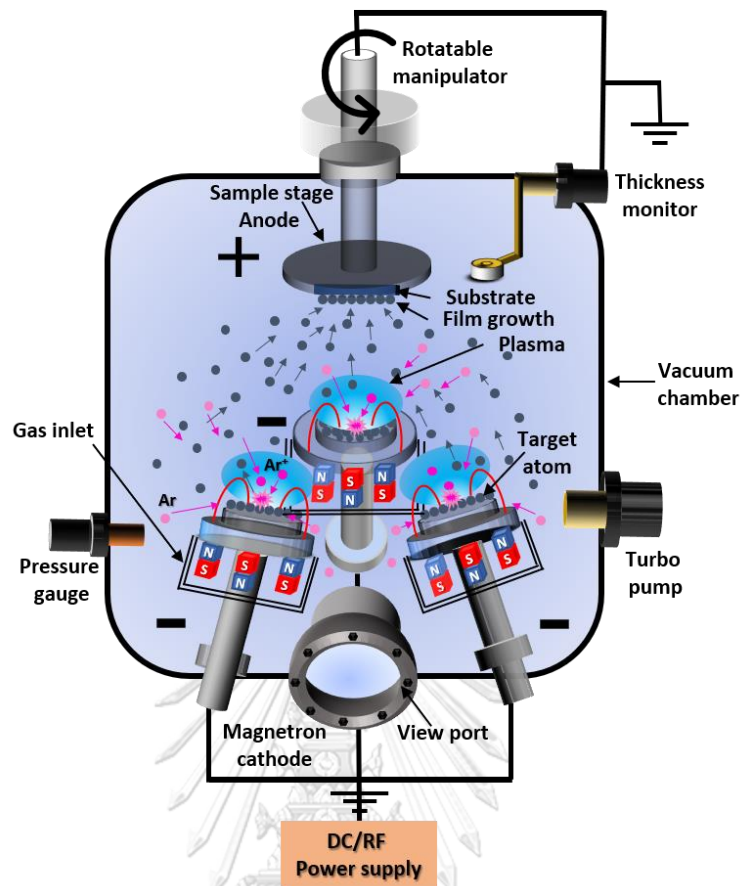


Figure 7 Schematic illustration of magnetron sputtering system [32].

2.3 Material characterization techniques

2.3.1 Field-Emission Scanning Electron Microscopy (FESEM)

The surface morphology and cross-section of the SnO₂ and perovskite films were investigated using FESEM (JEOL Model JSM-7001F). The basic element of FESEM includes an electron gun, a magnetic lenses, and an electron detector as shown in Figure 8 [33]. The electrons, produced by the electron gun with a source of electrons, are accelerated by an electric field through a combination of lenses into the electron beam. The focal length of lenses is adjusted by an objective lens for the electron beam to hit the surface of the sample. The second electrons generated by the scanning electron beam can be detected by the detectors.

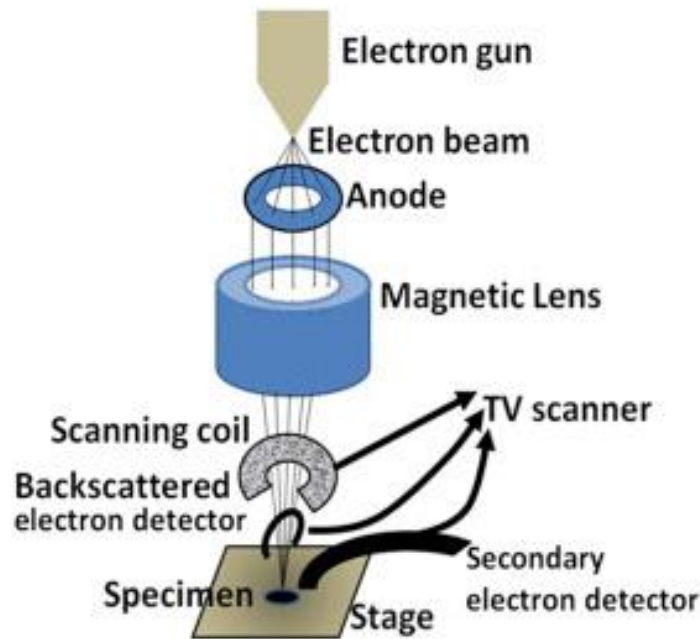


Figure 8 Schematic illustration of field-emission scanning electron microscopy (FESEM) [33].

2.3.2 Atomic Force Microscopy (AFM)

The AFM (Veeco Dimension 3100) was used to investigate the surface morphology and roughness of SnO₂ films. Measurements were made by the interaction between probe and sample surface. Figure 9 shows the basic element of AFM includes a cantilever with a sharp tip, a photodetector, a laser, and a feedback loop for detection. The probe was moved on a horizontal surface and then the movements of cantilever on a vertical bending were measured by a photodetector.

The surface roughness is calculated via the root mean squared (rms) value:

$$\text{rms - roughness } (R_q) = \sqrt{\frac{\sum_{i=1}^N (h_i - \bar{h})^2}{N}} \quad (2)$$

where h_i is the height at position i^{th} , \bar{h} is the average height, and N is the number of data points. The distances between the highest and lowest position are followed by z - range:

$$z - \text{range} = h_{\text{max}} - h_{\text{min}} \quad (3)$$

where h_{max} is the maximum height of surface and h_{min} is the minimum height of surface.

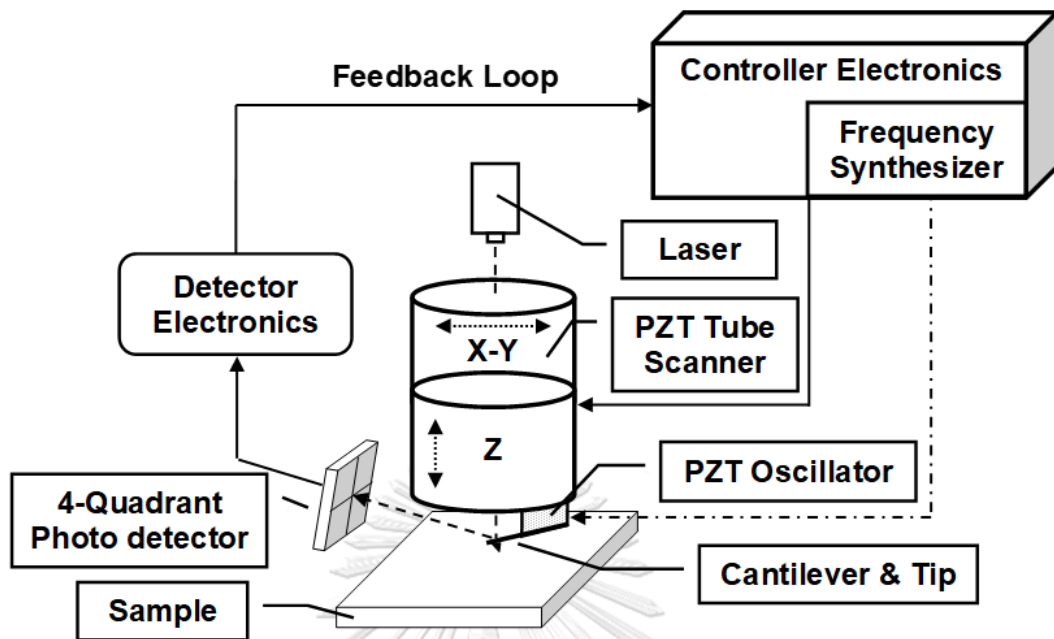
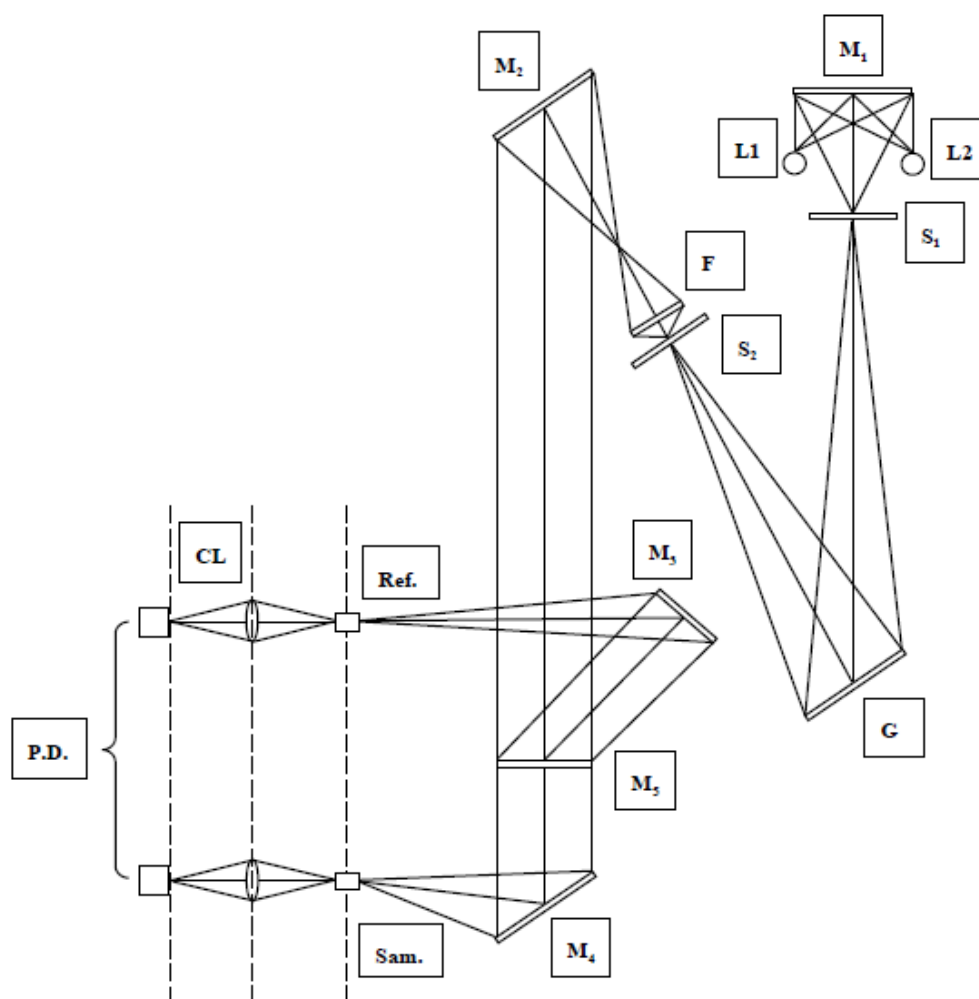


Figure 9 Schematic illustration of an atomic force microscope (AFM) [34].

2.3.3 Optical Transmission Spectroscopy

The UV-Vis-NIR spectrophotometer (Shimadzu Model UVPC1600) was used to investigate the responses of materials to the light absorption in the range from ultra-violet to infrared in terms of optical transmittance. The optical path of UV-Vis-NIR spectrophotometer is shown in Figure 10.



L1	Deuterium Lamp	L2	Halogen Lamp
F	Filter	G	Grating
S ₁	Entrance slit	S ₂	Exit slit
M ₁ – M ₄	Mirrors	M ₅	Half mirror
P.D.	Photo detector	Sam.	Cell for sample beam
Ref.	Cell for reference beam	CL	Convex lens

Figure 10 Schematic diagram showing optical paths of the UV-Vis-NIR spectrophotometer (Shimadzu Model UVPC1600).

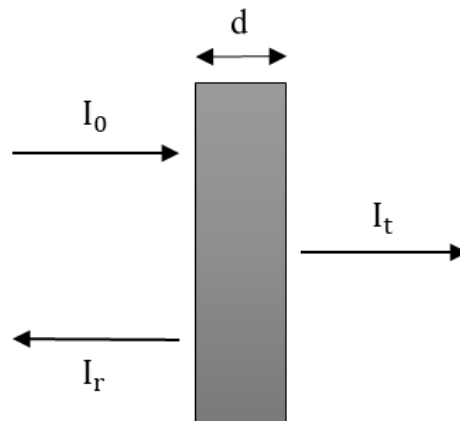


Figure 11 Schematic diagram of optical transmission and reflection in the thin film.

The schematic diagram of normal incidence of optical transmission and reflection in thin film is shown in Figure 11. The intensity (I) of light due to the absorption in the thin film is

$$I = I_0 e^{-\alpha x} \quad (4)$$

where x is the thickness of the thin film and α is the absorption coefficient. The optical transmission (T) and reflection (R) can be expressed in terms of the intensity of transmitted light (I_t), the intensity of reflected light (I_r), and the intensity of incident light (I_0), which can be written as

$$T = \frac{I_t}{I_0} \quad (5)$$

$$R = \frac{I_r}{I_0} \quad (6)$$

From Equations (5), the percentage of optical transmission (% T) can be written as

$$\%T = \frac{I_t}{I_0} \times 100 \quad (7)$$

The absorption is expressed in terms of the absorption coefficient can be obtained from

$$\alpha = -\frac{1}{d} \ln \left(\frac{\%T}{100} \right) \quad (8)$$

In addition, the absorption can be used to determine the band gap energy (E_g), which is the minimum energy that is required to excite an electron from the lower energy valence band to the higher energy conduction band. This is called an interband transition. For the thin films, the interband transition is the allowed direct transition:

$$\alpha h\nu = A(h\nu - E_g)^{\frac{1}{2}} \quad (9)$$

where A is constant, and $h\nu$ is the photon energy being expressed in eV.

2.3.4 Surface profiler

The Dektak³ST is a surface profile measuring system, which accurately measures a sample thickness. Measurements are made electromechanically by moving the stage below the diamond-tipped stylus according to parameters set by the user such as scan length and speed. As the stage moves the sample, surface variations are recorded. The graphic screen display exhibits data plot as shown in Figure 12.



Figure 12 Photograph of measurement result by Dektak³ST surface profiler.

2.3.5 Current density-voltage (J-V) measurement

The performances of PSCs were investigated through the current density-voltage (J-V) curves under AM 1.5 illumination with the light intensity of 100 mW/cm^2 using a Xe-lamp solar simulator and a Keithley 238 source-meter unit. The solar cell parameters are the open-circuit voltage (V_{oc}), the short-circuit current density (J_{sc}), the fill factor (FF), and the power conversion efficiency (PCE).

The fill factor (FF) can be calculated from the maximum output power density ($P_m = I_m V_m$), and can be written as

$$FF = \frac{I_m V_m}{I_{sc} V_{oc}}. \quad (10)$$

The power conversion efficiency (PCE) is the ratio of the maximum output power density (P_m) and the incident light power density (P_i), which is defined as

$$PCE = \frac{I_m V_m}{P_i}. \quad (11)$$

From Equations (10) and (11), the PCE can be obtained from

$$PCE = \frac{I_{sc} V_{oc} FF}{P_i}. \quad (12)$$

CHAPTER III

FABRICATION AND CHARACTERIZATION OF THE SnO₂ AND PEROVSKITE SOLAR CELLS

In this chapter, the fabrication and characterization of the SnO₂ films and perovskite solar cells (PSCs) are described.

3.1 Perovskite solar cells fabrication

The normal planar structure of PSCs in this work consists of five layers, i.e., transparent electrode (FTO), electron transport layer (ETL), perovskite absorber layer, hole transport layer (HTL), and metal electrode as shown in Figure 13.

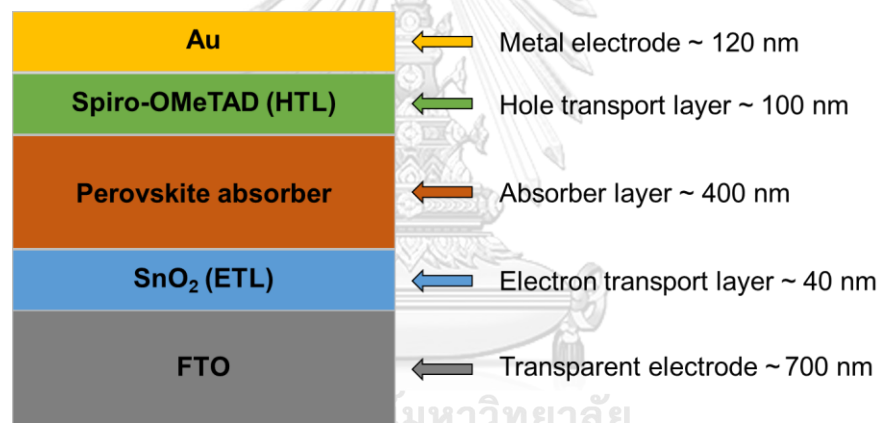


Figure 13 Schematic diagram of the normal planar structure of PSCs.

3.1.1 Substrate preparation

The 3 cm × 3 cm Fluorine-doped tin oxide (FTO) substrates were chemically etched with Zn powder and hydrochloric acid (HCl). The patterned FTO substrate was covered with polyimide tape during etching as shown in Figure 14. The sheet resistance of FTO substrate was 18 Ω/sq and the thickness of FTO film and glass substrate are approximately 700 nm and 3 mm, respectively. The FTO substrates were ultrasonically cleaned with detergent (Micro 90) in deionized (DI) water, DI water, acetone, and 2-propanol (IPA) for 30 min, respectively. Finally, the FTO substrates were dried with N₂ gas and kept in a desiccator prior to the depositions of PSCs.

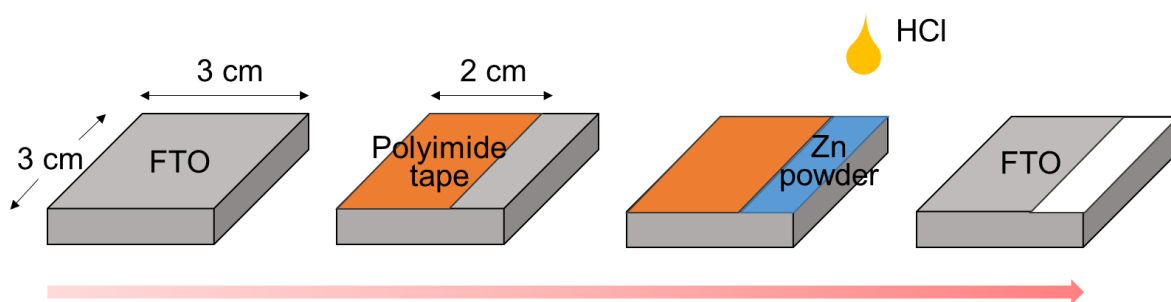


Figure 14 Schematic diagrams of preparation with FTO substrate for transparent electrode.

3.1.2 Fabrication of SnO₂ films

In this work, SnO₂ films as ETL were fabricated by spin-coating and RF magnetron sputtering techniques.

3.1.2.1 SnO₂ films by spin-coating method

Part of FTO substrate was covered with polyimide tape to deposit SnO₂ as shown in Figure 15. The surface treatment of the FTO substrates was done by UV-ozone for 10 min prior to the deposition of SnO₂. For spin-coating method (Figure 16), the SnO₂ film was deposited using either SnCl₂·2H₂O (99.99%, Sigma-Aldrich) or SnCl₄·5H₂O (98%, Sigma-Aldrich) dissolved in ethanol and IPA (99.5%, Sigma-Aldrich) and stirred for 12 hrs. The SnO₂ solution (300 μl) was spin-coated on the FTO substrates with various precursor concentration and spin speed for 40 s. After that, the SnO₂ films were annealed on a hotplate at 200 °C for 60 min and 250 °C for 30 min in air.

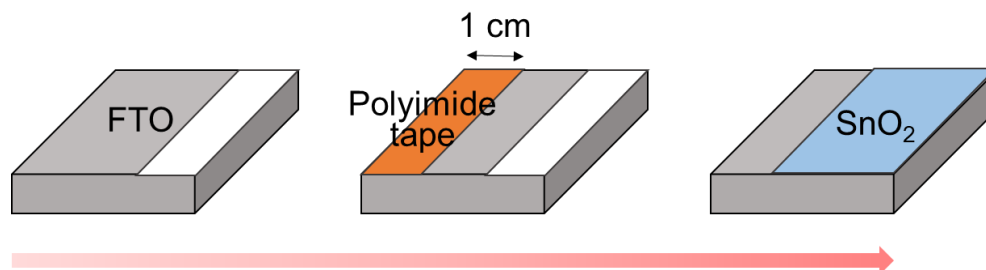


Figure 15 Schematic diagrams of preparation with SnO₂ films for ETL.

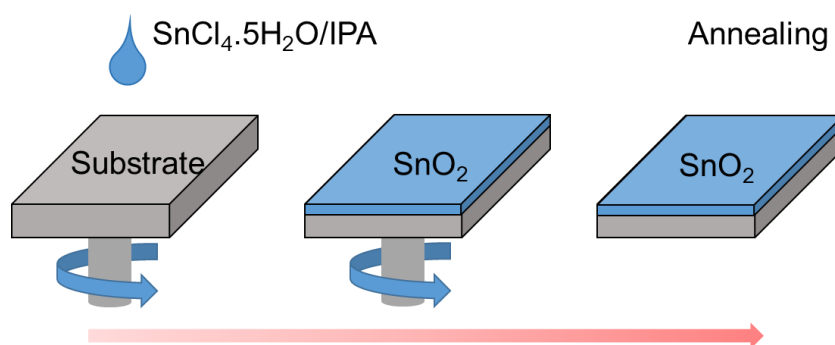


Figure 16 Schematic diagrams showing spin-coating method of SnO₂ films.

3.1.2.2 SnO₂ films by RF magnetron sputtering technique

The SnO₂ film was deposited on FTO substrate by covering the substrate with polyimide tape similar to that shown in Figure 15. For RF sputtering technique, Ar (99.999% purity) and O₂ (99.999% purity) gas was used during sputtering process by using a SnO₂ sputtering target (99.99%, 100 mm diameter, 5 mm thickness) as shown in Figure 17. The FTO substrates were placed on a substrate holder in a chamber and the target and substrate distance was 6 cm. The deposition process started after the chamber was evacuated to a base pressure of 3×10^{-6} mbar. The substrates were rotated above target at the rate of 3 rpm. The deposition time was varied from 52 min to 210 min, RF sputtering power was varied from 60 W to 150 W, the Ar sputtering gas pressure was varied from 1×10^{-3} mbar to 6×10^{-3} mbar while keeping O₂ partial pressure at 1.5×10^{-4} mbar.

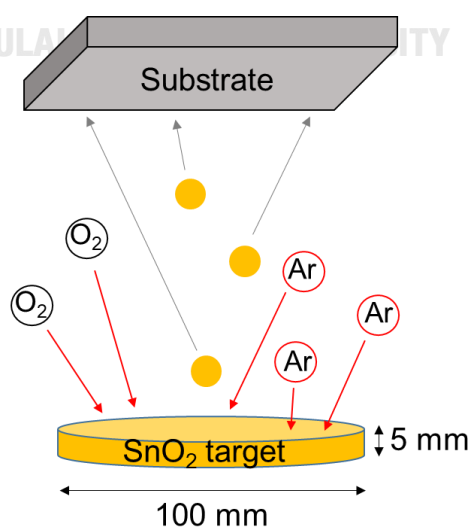


Figure 17 Schematic diagram showing the RF magnetron sputtering deposition process. Ar and O₂ gas were used during sputtering process.

3.1.3 Fabrication of TiO₂ films

In this work, the TiO₂ compact layer (cp-TiO₂) and TiO₂ mesoporous layer (mp-TiO₂) as the ETLs were fabricated by spin-coating method.

3.1.3.1 TiO₂ compact layer (cp-TiO₂)

The FTO substrate was firstly covered with polyimide tape as shown in Figure 18. The substrate was treated with UV-ozone for 10 min prior to the deposition of ETL. The compact TiO₂ solution was prepared from 1 ml TiO₂ blocking layer (Greatcell Solar) dissolved in 2 ml of ethanol and stirred at 70 °C for 12 hrs. The compact TiO₂ solution (400 μl) was deposited on the FTO substrate by spin-coating at 3000 rpm for 30 s in N₂-filled glovebox, and then annealed on a hotplate at 500 °C for 30 min in air.

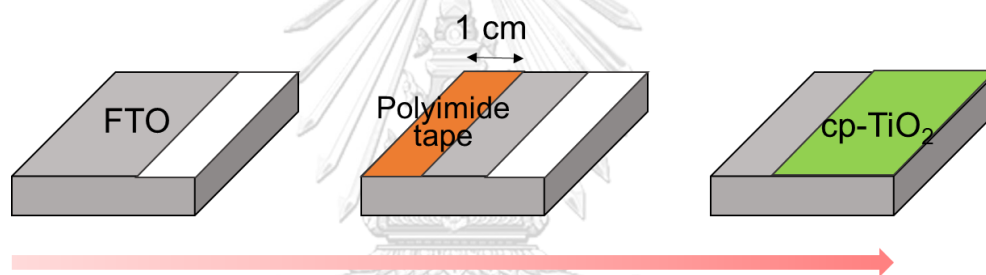


Figure 18 Schematic diagrams of preparation with cp-TiO₂ layers for ETLs.

3.1.3.2 TiO₂ mesoporous layer (mp-TiO₂)

The cp-TiO₂ layer was then covered with polyimide tape as shown in Figure 19. The cp-TiO₂ layer was treated by UV-ozone for 10 min prior to the deposition of mesoporous layer. The mesoporous TiO₂ layer was deposited by spin-coating method in N₂-filled glovebox using 1ml TiO₂ paste (30NR-D, Greatcell Solar) dissolved in 7 ml of ethanol and stirred for 12 hrs. The mesoporous TiO₂ solution (400 μl) was spin-coated on the cp-TiO₂ layer at 3000 rpm for 30 s. After that, the mp-TiO₂ layer was annealed on a hotplate at 500 °C for 30 min in air.

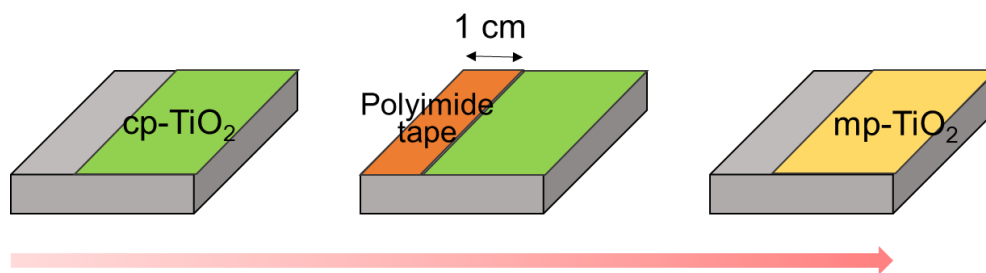


Figure 19 Schematic diagrams of preparation with mp-TiO₂ layers for ETLs.

3.1.4 Fabrication of perovskite absorber layer

The ETL film, either SnO₂ or TiO₂, was treated with UV-ozone for 10 min to improve its hydrophilicity. The MAPbI₃ perovskite thin film was deposited by the two-step spin-coating method in N₂-filled glovebox as shown in Figure 20. The PbI₂ solution was prepared from 0.461 g PbI₂ (99.999%, Sigma-Aldrich) dissolved in 1 ml of N,N-Dimethylformamide (DMF, 99.8%, Sigma-Aldrich) and N,N-Dimethylsulfoxide (DMSO, 99.9%, Sigma-Aldrich) with 4:1 by volume and stirred at 70 °C for 12 hrs. Before depositing perovskite layer, the SnO₂ substrates were preheated on a hotplate at 70 °C for 10 min. The PbI₂ solution (200 μl) was deposited on the preheated SnO₂ by spin-coating at 3000 rpm for 30 s, and then annealed on a hotplate at 70 °C for 20 min. After that, the solution (400 μl) of methylammonium iodide (MAI, Dyesol) which consists of 0.010 g MAI dissolved in 1 ml of IPA and stirred for 12 hrs was spin-coated on the PbI₂ layer at 2000 rpm for 20 s. In order to obtain a high quality perovskite absorber layer, the anti-solvent (50 μl) of chlorobenzene (CB, 99.8%, Sigma-Aldrich) was dropped while spin-coating the MAI layer. All the perovskite layers were annealed on a hotplate at 120 °C for 10 min.

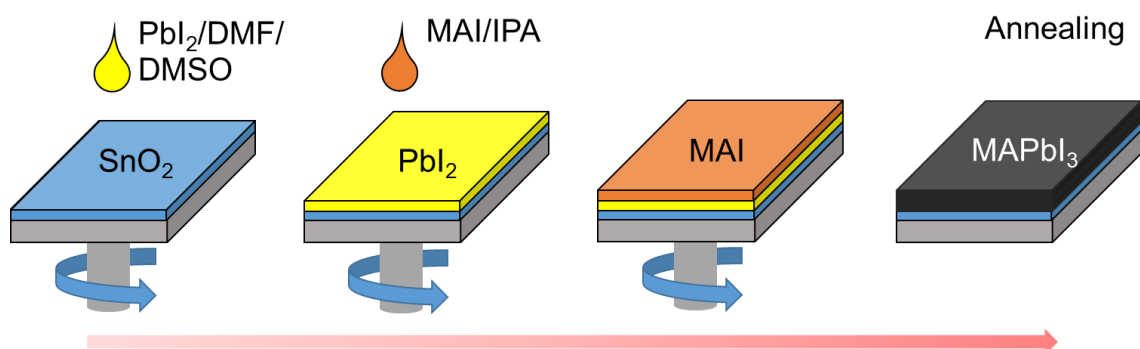


Figure 20 Schematic diagrams of two-step spin-coating method to deposit MAPbI₃ perovskite films.

3.1.5 Fabrication of hole transport layer

The HTL was deposited on top of the perovskite layer using Spiro-OMeTAD solution which was prepared from dissolving 0.0723 g of Spiro-OMeTAD (99.8%, Borun New Material Technology Ltd.) into 1 ml of CB and 28.8 μ l of 4-tert-butylpyridine (t-BP, 96%, Sigma-Aldrich) and 17.5 μ l of lithium bistrifluoromethanesulfonimide (Li-TFSI, 99% ,Sigma-Aldrich) (pre-dissolved as 520 mg/ml solution in acetonitrile, 99.8%, Sigma-Aldrich) and stirred for 12 hrs. 150 μ l of Spiro-OMeTAD solution was dropped and spin-coated on the perovskite layer at 3000 rpm for 30 s. It was worthy to note that the perovskite absorber layer and HTL process were carried out inside the N₂-filled glovebox (Figure 21). Finally, the perovskite absorber and Spiro-OMeTAD layer, closing area of 1 cm \times 3 cm polyimide tape, were cleaned with DMF for making electrode. The films were kept in a low vacuum pot overnight to oxidize Spiro-OMeTAD.



Figure 21 Photograph of the N₂-filled glovebox (Changsha Tianchuang Powder Technology Co., Ltd.).

3.1.6 Fabrication of Au metal electrode

The Au metal electrode was deposited on the Spiro-OMeTAD layer by thermal evaporation with thickness of 120 nm using a shadow mask as shown in Figure 22. The

deposition process start after the chamber was evacuated to a base pressure of 9.8×10^{-6} mbar.



Figure 22 Photograph of a shadow mask for Au metal electrode.

3.2 Characterizations

The thin film layers as well as the PSCs fabricated in this work were characterized by field-emission scanning electron microscopy (FESEM), atomic force microscopy (AFM), optical transmission spectroscopy, surface profiler, and current density-voltage (J-V) measurement.

3.2.1 Field-Emission Scanning Electron Microscopy (FESEM)

The FESEM (JEOL Model JSM-7001F) was used to investigate the surface morphology and cross-section of the SnO₂ and perovskite films. It was used to study microstructures or nanostructures of films. The surface morphology and cross-section were imaged with magnification of X5,000 to X50,000. In addition, the material compositions of the SnO₂ films were investigated using energy dispersive spectroscopy (EDS).

3.2.2 Atomic Force Microscopy (AFM)

The AFM (Veeco Dimension 3100) was used to observe the surface morphology and the roughness of the SnO₂ films on soda-lime glass (SLG) substrates. The surface area of imaging was 5 μm × 5 μm. AFM was also used to measure the root mean square (rms) roughness.

3.2.3 Optical Transmission Spectroscopy

The transmittance and absorbance spectra of the SnO₂ films and perovskite absorber layer were investigated in the range of 330 nm to 1100 nm by a UV-Vis-NIR spectrophotometer (Shimadzu Model UVPC1600).

3.2.4 Surface profiler

The thickness of the SnO₂ films was measured by Dektak³ST surface profiler. In this work, the SnO₂ film was deposited on SLG substrate by covering the substrate with polyimide tape as shown in Figure 23.

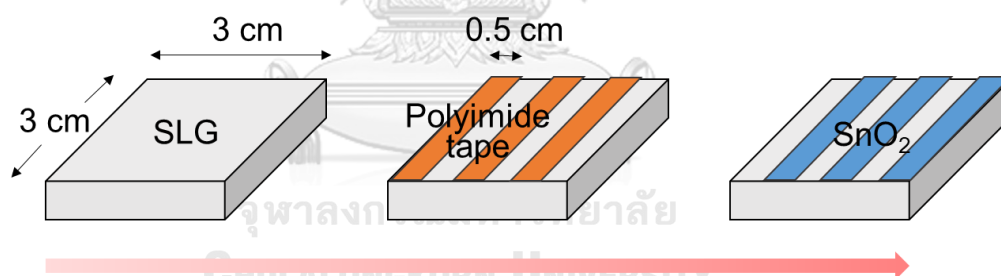


Figure 23 Schematic diagrams of preparation with SnO₂ films for thickness measurement by Dektak³ST surface profiler.

3.2.5 Current density-voltage (J-V) measurement

The J-V curves of the PSCs were measured under AM 1.5 illumination with the light intensity of 100 mW/cm² using a Xe-lamp solar simulator and a Keithley 238 source-meter unit. The solar cell parameters are the open-circuit voltage (V_{oc}), the short-circuit current density (J_{sc}), the fill factor (FF), and the power conversion efficiency (PCE). The PSC devices under investigation have an active area of 0.06 and 0.2 cm².

CHAPTER IV

RESULTS AND DISCUSSION

In this chapter, the results of the SnO₂ films and perovskite solar cells (PSCs) are discussed in terms of surface morphology, optical transmission, electrical properties, and J-V characteristics. The discussions of the effects of electron transport layer (ETL) on the performance of the PSCs are described.

4.1 Characteristics of spin-coated SnO₂ films

4.1.1 The surface morphology of spin-coated SnO₂ films

The morphology of SnO₂ film deposited on SLG substrates by spin-coating method is shown in FESEM image. The SnO₂ films fully cover the SLG substrates. The EDS measurement was used for inspection of the elemental composition of the films. Figure 24 shows the FESEM image and the EDS spectrum of SLG substrate. It can be seen that the SLG substrate has smooth surface and the composition consists of Sn (0.20 Atomic %), O (77.05 Atomic %), Si (15.46 Atomic %), Na (5.05 Atomic %), Mg (1.45 Atomic %), and Ca (0.78 Atomic %). Figure 25 illustrates the FESEM image and the EDS spectrum of the SnO₂ films on the SLG substrates and the composition consists of Sn (1.09 Atomic %) and O (68.93 Atomic %) when other elements, such as Si, Na, Mg, and Ca, are included in the SLG compositions. However, it can be seen that when SnO₂ precursor was deposited by wet chemical process, some particulates from recrystallization of SnCl₄ precursor were observed on some area of SnO₂ surface. The EDS spectrum shows material composition of Sn (2.15 Atomic %), Cl (1.26 Atomic %), and O (62.92 Atomic %) in the area of some particles as shown in Figure 26 (b). However, the atomic percentage of oxygen is not accurate for the composition of SnO₂ films since the EDS has an effective probe depth about 1 μm, which is deeper than the thickness of SnO₂ films (~ 60 nm).

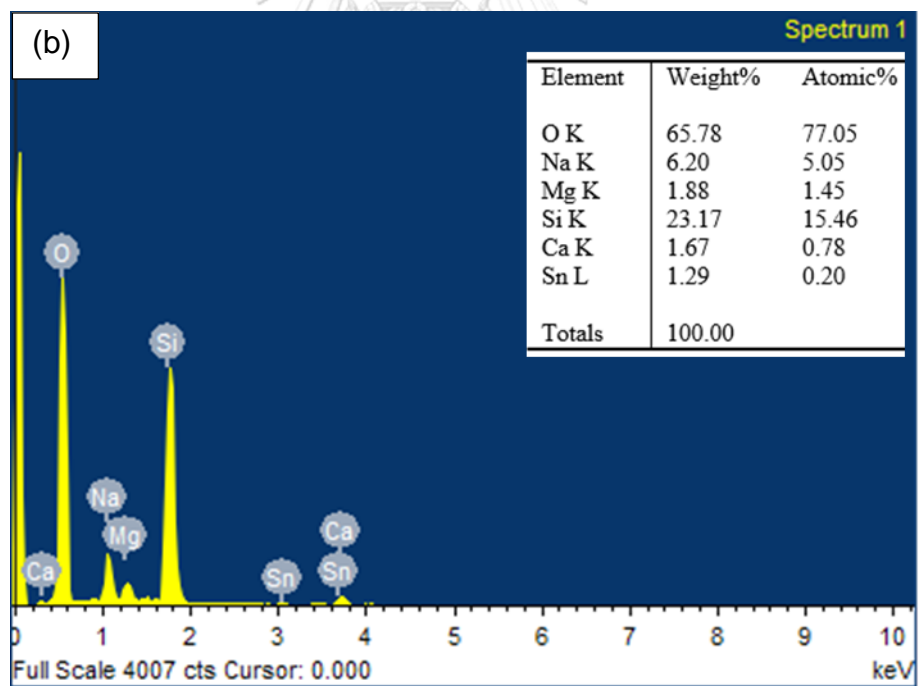
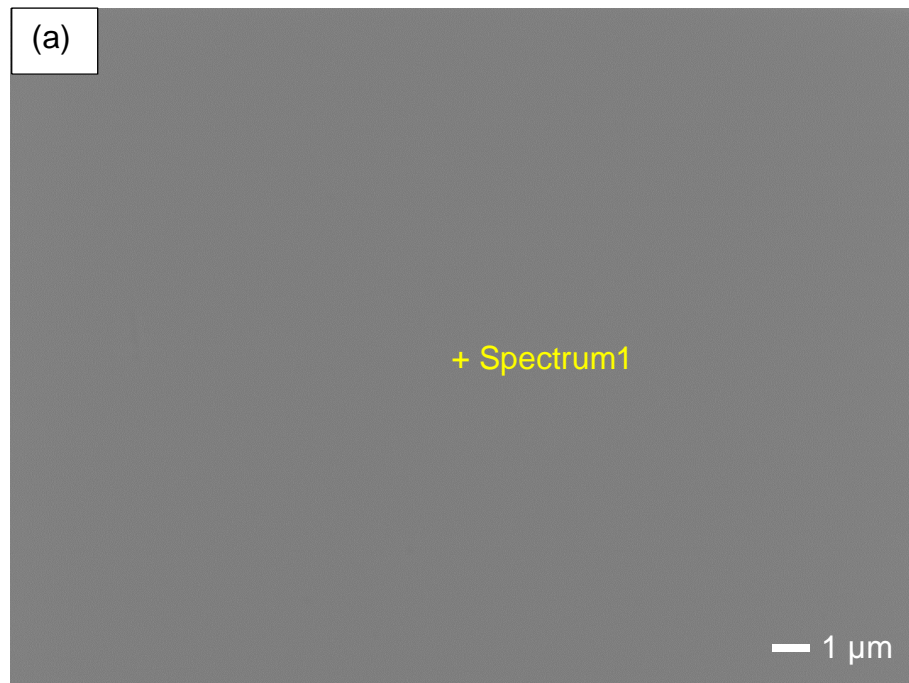


Figure 24 (a) FESEM image and (b) EDS spectrum of SLG substrate.

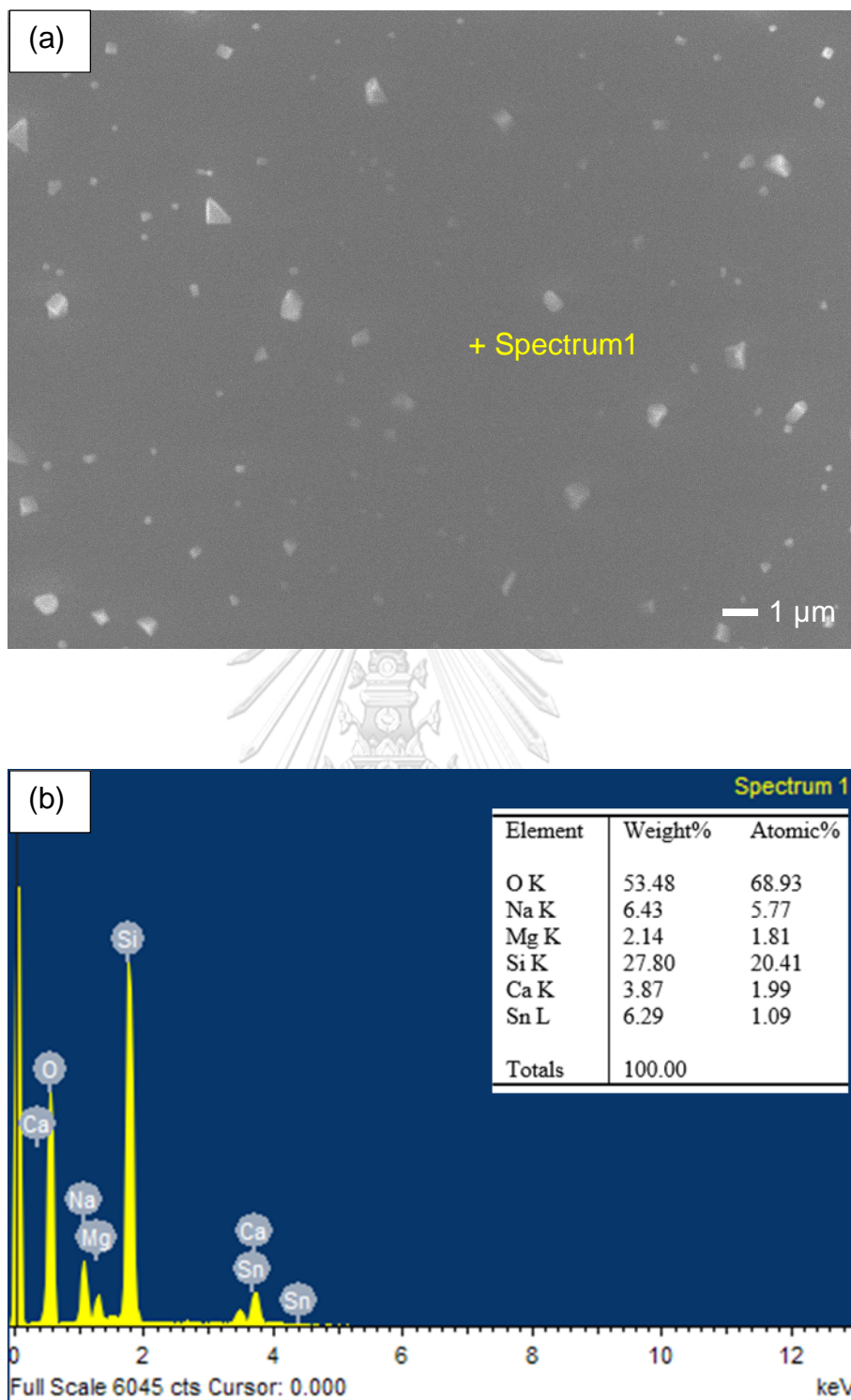


Figure 25 (a) FESEM image and (b) EDS spectrum of spin-coated SnO₂ film on SLG substrate without particle in the SnO₂ surface.

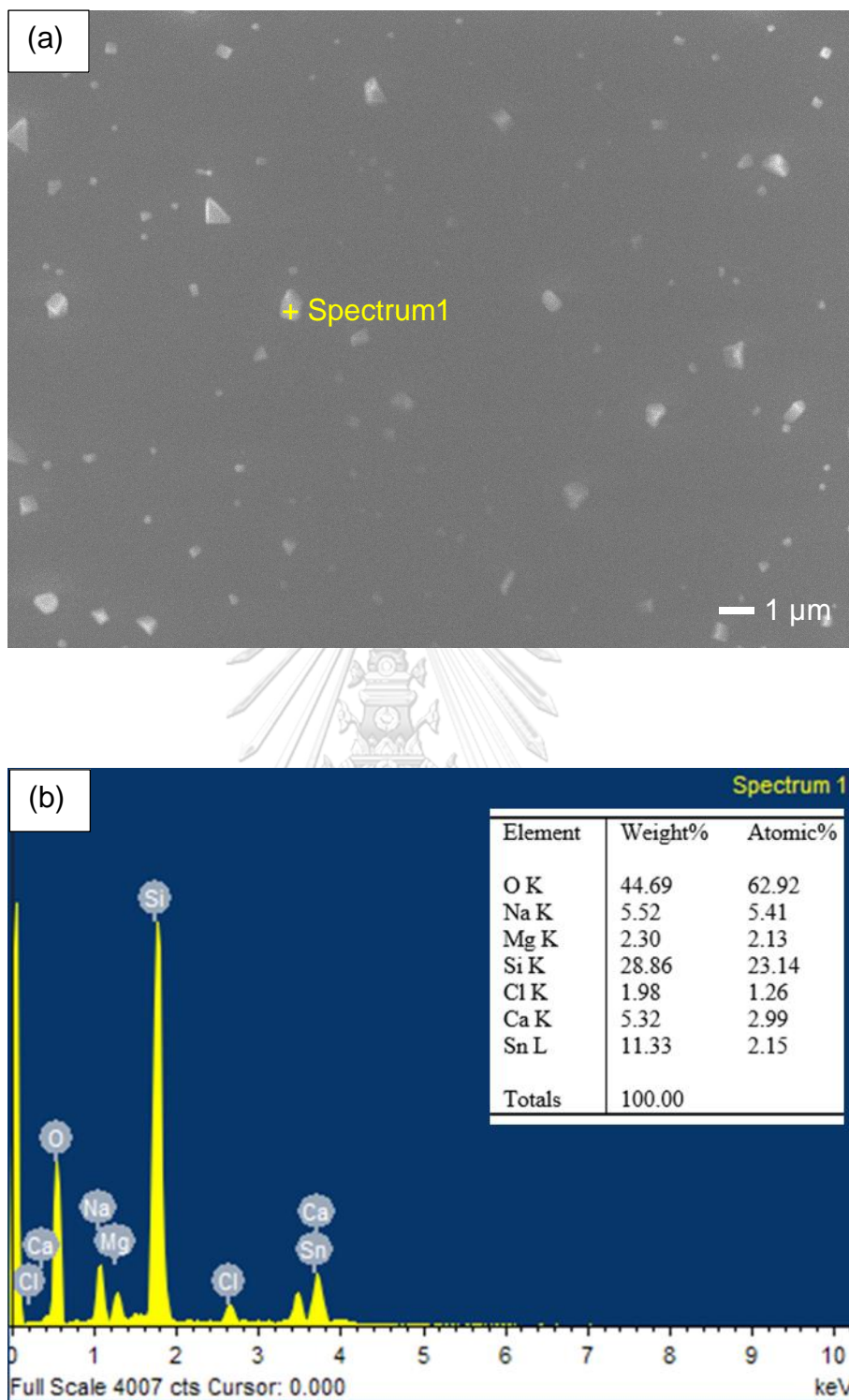


Figure 26 (a) FESEM image and (b) EDS spectrum of spin-coated SnO₂ film on SLG substrate with particle in the SnO₂ surface.

The effects of spin-coating parameters were considered for the SnO₂ films using SnCl₄.5H₂O and SnCl₂.2H₂O precursors with various precursor concentration ranging from 0.05 M to 0.7 M while keeping spin speed at 3000 rpm for 40 s. Figure 27 presents the FESEM images of the SnO₂ films deposited with 0.1 M and 0.15 M SnCl₄.5H₂O in IPA. There is no particulate on the surfaces of these uniform SnO₂ layer. It can be seen in Figure 28 and Figure 29, using SnCl₂.2H₂O dissolved in ethanol, that both small grains of SnCl₄ precursor were formed at low concentration. On the other hand, at higher concentration, it was found that the SnO₂ surface was very smooth.

Table 1 and Table 2 illustrate the FESEM images of the SnO₂ films using SnCl₅.4H₂O precursor with various spin speed from 2000 rpm to 5000 rpm for 40 s. The FESEM images show that the SnO₂ surfaces do not change significantly with spin speed and the surface becomes smoother with increase concentration.

In order to investigate the effect of the SnO₂ surfaces using SnCl₂.2H₂O precursor with various spin speeds of 2000, 3000, 4000, and 5000 rpm for 40 s. It is compared and showed in Table 3 and Table 4 that the FESEM images of the SnO₂ film on SLG substrates show more uniform particulates from recrystallization of SnCl₄ precursor on surfaces and no difference for various spin speeds.

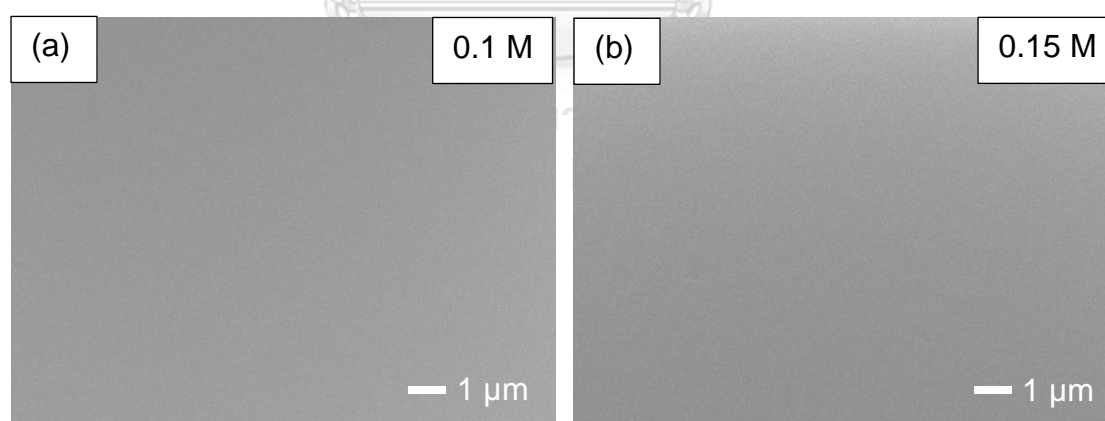


Figure 27 FESEM images of spin-coated SnO₂ film on SLG substrates using SnCl₄.5H₂O dissolved in IPA with varying precursor concentration (a) 0.1 M and (b) 0.2 M while keeping spin speed at 3000 rpm for 40 s and annealing on a hotplate at 250 °C for 30 min.

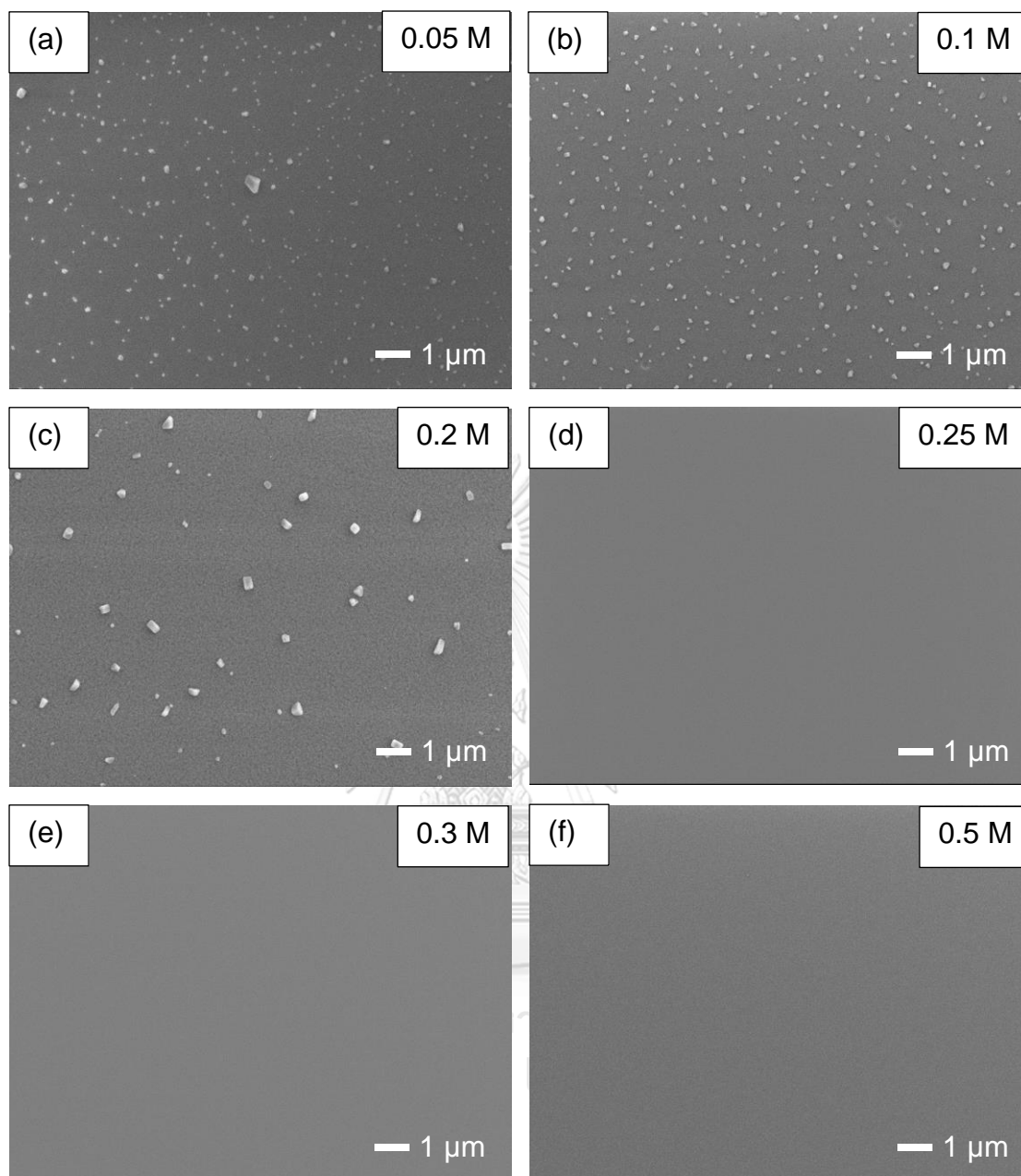


Figure 28 FESEM images of spin-coated SnO₂ film on SLG substrates using SnCl₂·2H₂O dissolved in ethanol with varying precursor concentration (a) 0.05 M, (b) 0.1 M, (c) 0.2 M, (d) 0.25 M, (e) 0.3 M, and (f) 0.5 M while keeping spin speed at 3000 rpm for 40 s and annealing on a hotplate at 200 °C for 60 min.

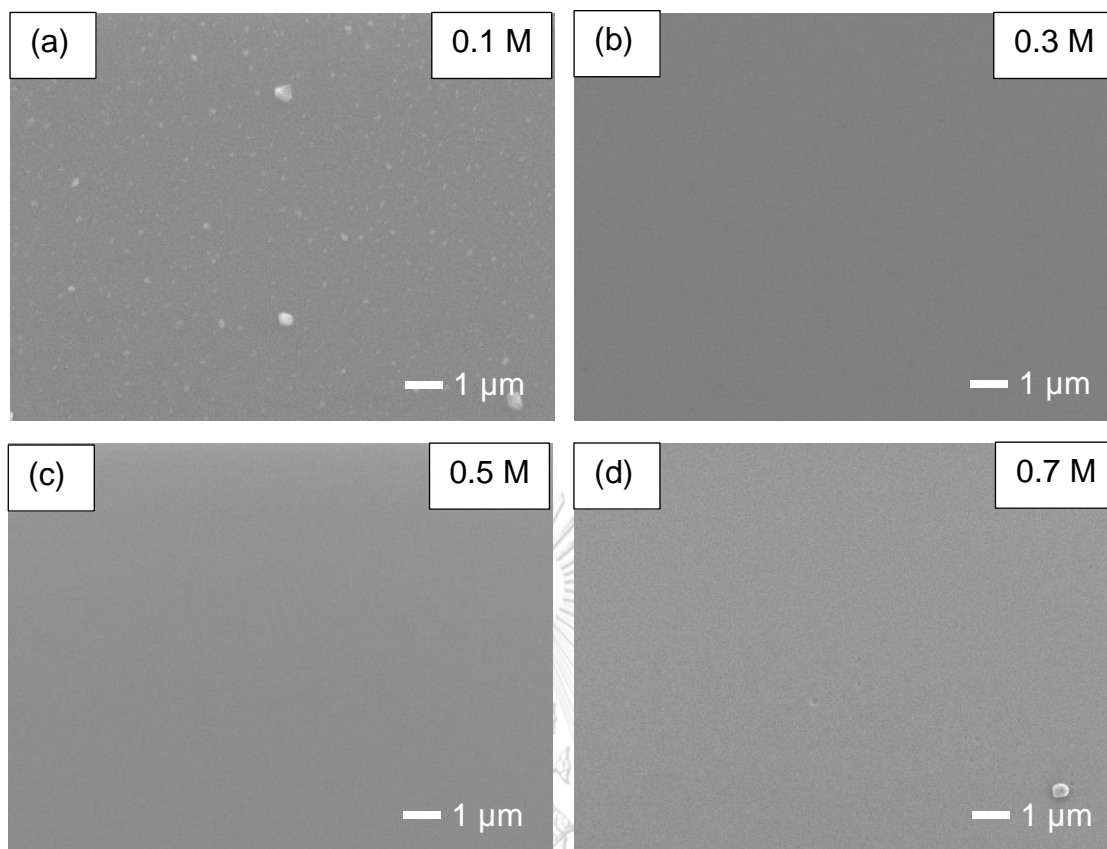


Figure 29 FESEM images of spin-coated SnO₂ film on SLG substrates using SnCl₂·2H₂O dissolved in ethanol (preheat solution) with varying precursor concentration (a) 0.1 M, (b) 0.3 M, (c) 0.5 M, and (d) 0.7 M while keeping spin speed at 3000 rpm for 40 s and annealing on a hotplate at 200 °C for 60 min.

Table 1 FESEM images of spin-coated SnO₂ film on SLG substrates using SnCl₄·5H₂O dissolved in ethanol with annealing on a hotplate at 200 °C for 60 min.

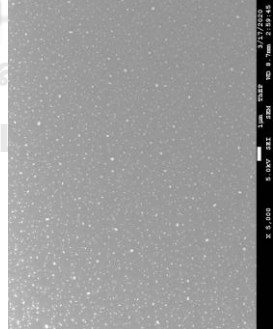
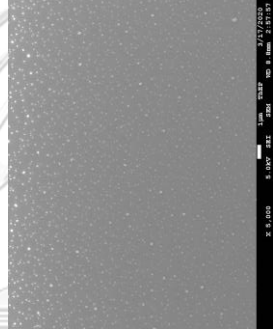
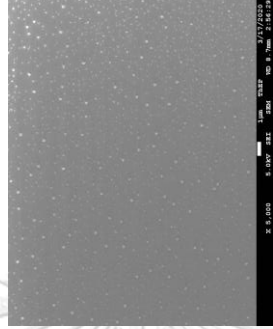
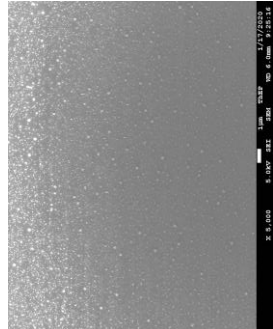
Concentration	Spin speed (rpm)			
0.1 M	2000	3000	4000	5000
				

Table 2 FESEM images of spin-coated SnO₂ film on SLG substrates using SnCl₄·5H₂O dissolved in IPA with annealing on a hotplate at 250 °C for 30 min.

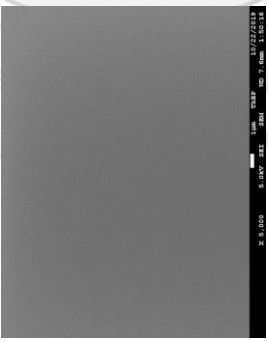
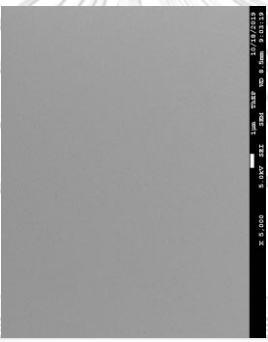
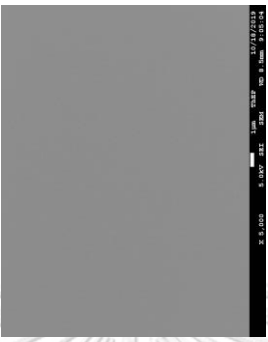

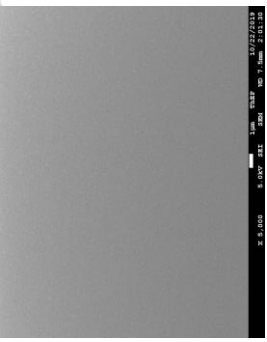
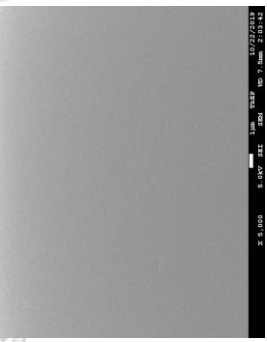
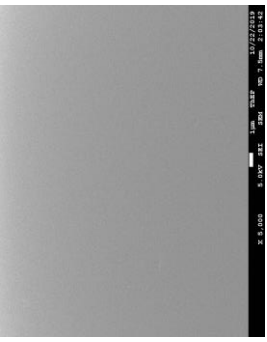
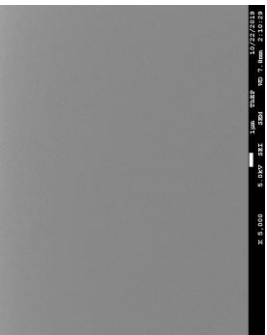
Concentration	Spin speed (rpm)			
	2000	3000	4000	5000
0.1 M				
0.2 M				

Table 3 FESEM images of spin-coated SnO₂ film on SLG substrates using SnCl₂·2H₂O dissolved in ethanol with annealing on a hotplate at 200 °C for 60 min.

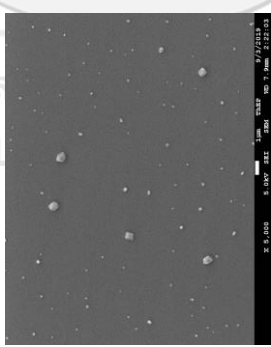
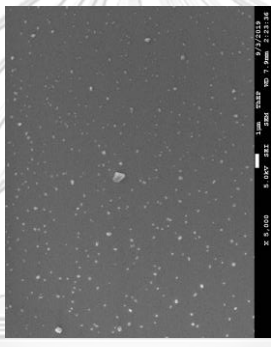
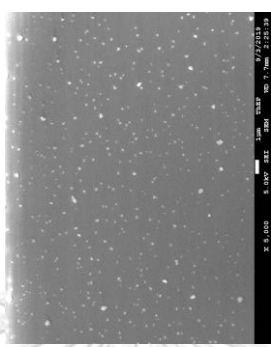
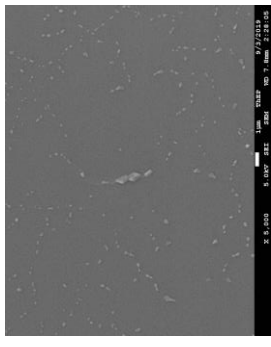
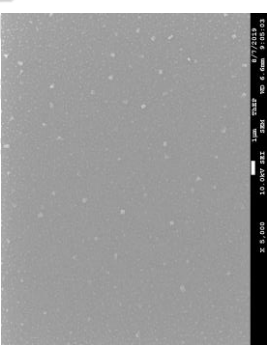
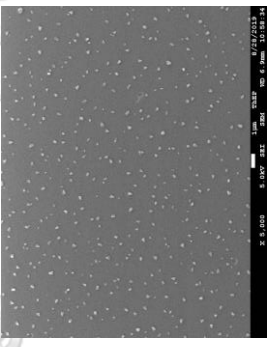
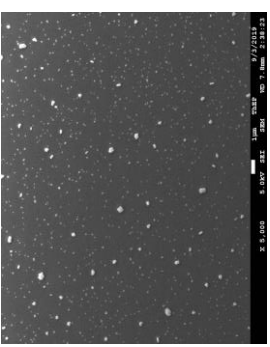
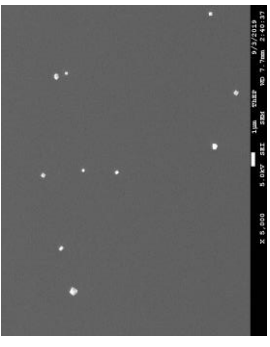
Concentration	Spin speed (rpm)			
	2000	3000	4000	5000
0.05 M				
0.1 M				

Table 3 FESEM images of spin-coated SnO_2 film on SLG substrates using $\text{SnCl}_2 \cdot 2\text{H}_2\text{O}$ dissolved in ethanol with annealing on a hotplate at 200°C for 60 min.


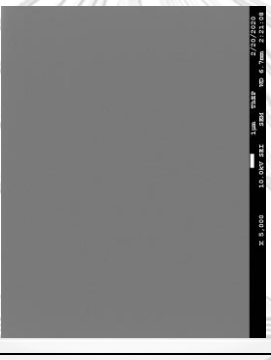



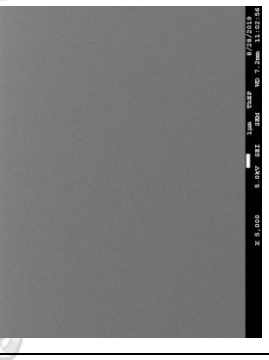
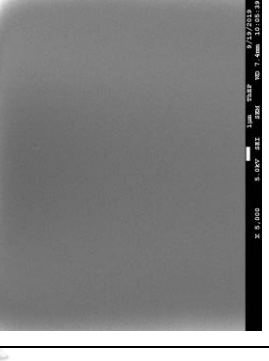
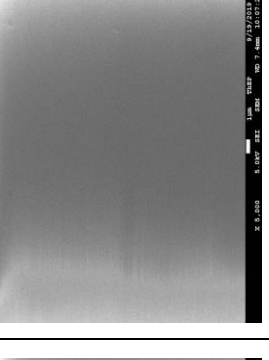
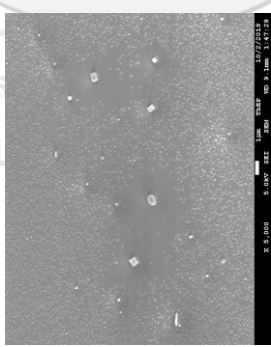
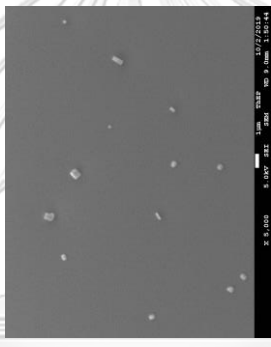
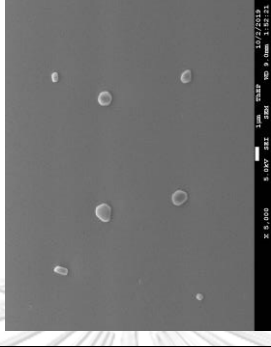
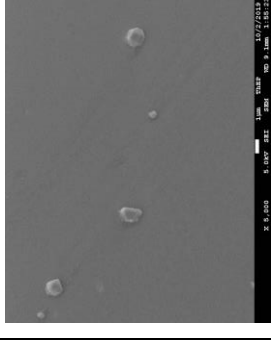
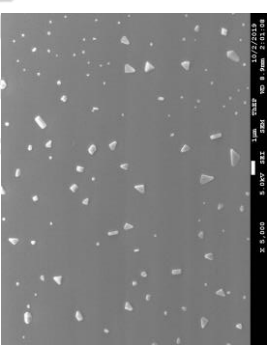
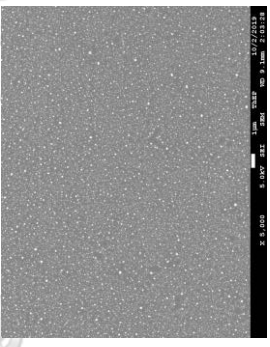
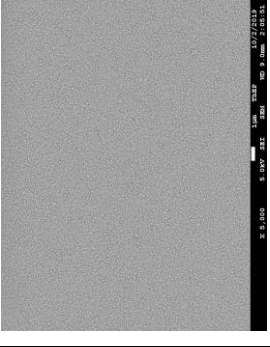
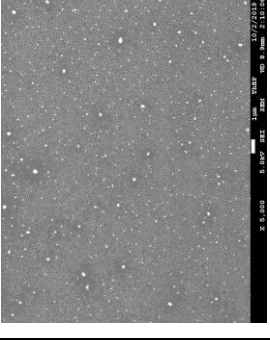
Concentration	Spin speed (rpm)			
	2000	3000	4000	5000
2.5 M				
0.5 M				

Table 4 FESEM images of spin-coated SnO_2 film on SLG substrates using $\text{SnCl}_2 \cdot 2\text{H}_2\text{O}$ dissolved in IPA with annealing on a hotplate at 250°C for 30 min.

Concentration	Spin speed (rpm)			
	2000	3000	4000	5000
0.1 M				
0.2 M				

4.1.2 The optical transmission spectrum of spin-coated SnO₂ films

The optical transmission spectrum of spin-coated SnO₂ films on SLG substrates using SnCl₄.5H₂O dissolved in IPA on different precursor concentration is shown in Figure 30. The spectrum did not change much in the optical transmission with the increase of precursor concentration. The optical transmission in the visible region (380 – 780 nm) was approximately > 90%.

Figure 31 illustrates the variation of the optical transmission spectrum of spin-coated SnO₂ films on SLG substrates using SnCl₂.2H₂O dissolved in ethanol on different precursor concentration. The results show that the 0.5 M of SnO₂ solution owns the highest optical transmission of 90% followed by 0.1 M (88%) and 0.2 M (85%) of SnO₂ solution.

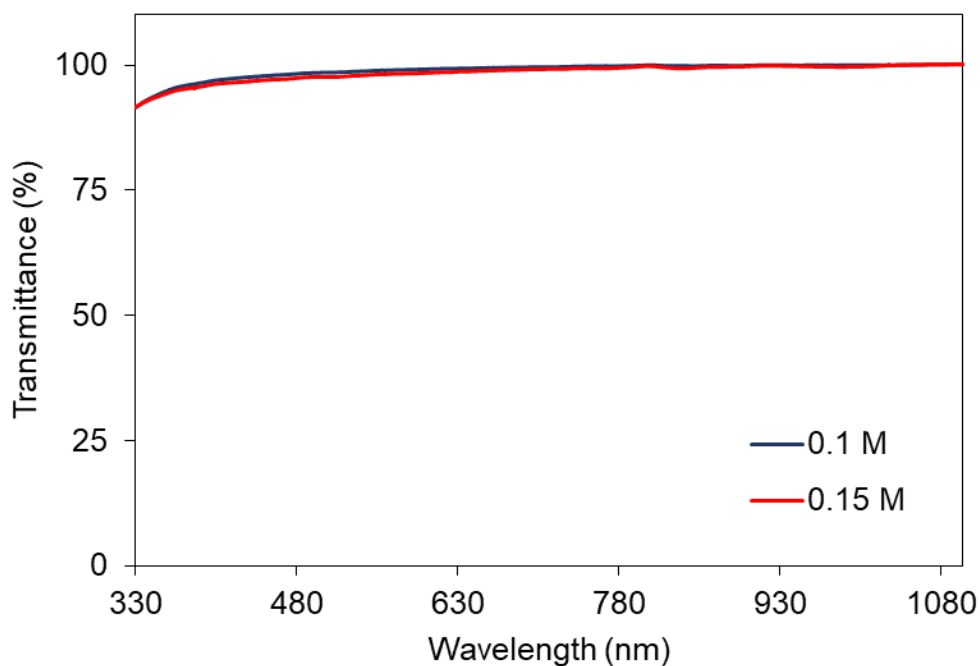


Figure 30 Optical transmission spectrum of spin-coated SnO₂ film on SLG substrates using SnCl₄.5H₂O dissolved in IPA with varying precursor concentration while keeping spin speed at 3000 rpm for 40 s and annealing on a hotplate at 200 °C for 60 min.

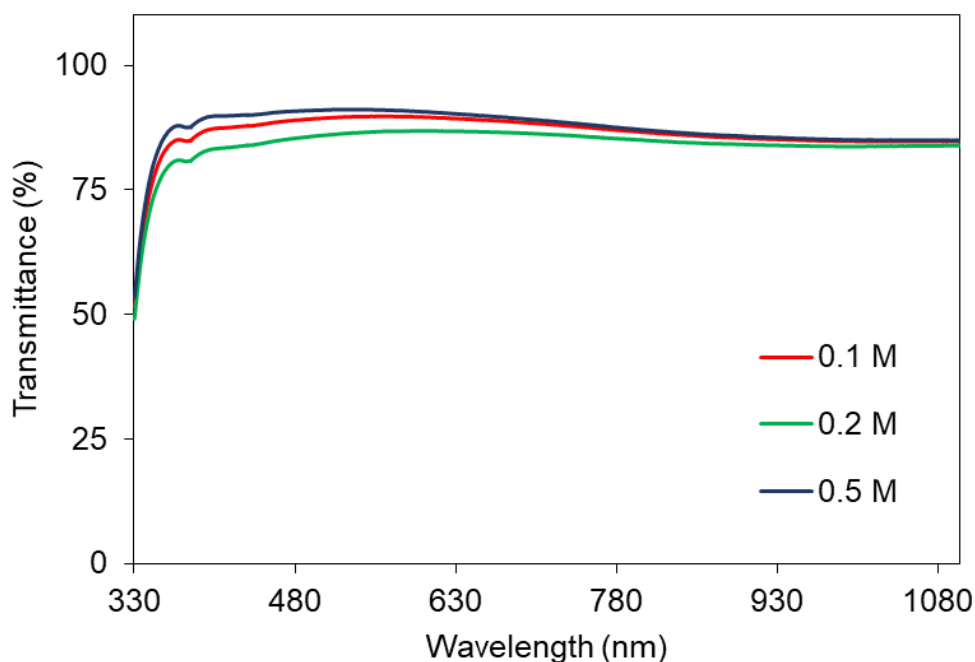


Figure 31 Optical transmission spectrum of spin-coated SnO₂ film on SLG substrates using SnCl₂·2H₂O dissolved in ethanol with varying precursor concentration while keeping spin speed at 3000 rpm for 40 s and annealing on a hotplate at 200 °C for 60 min.

4.2 Characteristics of sputtered SnO₂ films

4.2.1 The surface morphology of sputtered SnO₂ films

FESEM image of surface morphology of sputtered SnO₂ films on SLG substrate shows very smooth surface as shown in Figure 32. However, the FESEM images show no difference between SnO₂ films and SLG substrates. The sputtered SnO₂ films on SLG substrate show some small grains on some area of surface as seen in the AFM images. AFM images of SnO₂ films fabricated with 90 W sputtering power shows more uniform grains than that of 60 W as shown in Figure 33 and Figure 34. The rms roughness of the SLG substrate was 2.08 ± 0.20 nm. In order to study the effect of sputtering power on the sputtered SnO₂ films, the rms roughness of 60 W RF sputtering power with 40 nm thickness of SnO₂ films on SLG substrate was 3.35 ± 0.15 nm and 80 nm thickness of SnO₂ films on SLG substrate was higher at 5.27 ± 0.15 nm. The

SnO₂ film was deposited with 90 W RF sputtering power, which thickness of 35 nm, yielded rms roughness of 5.96 ± 0.15 nm.



Figure 32 FESEM image shows smooth surface morphology of sputtered SnO₂ film on SLG substrate.

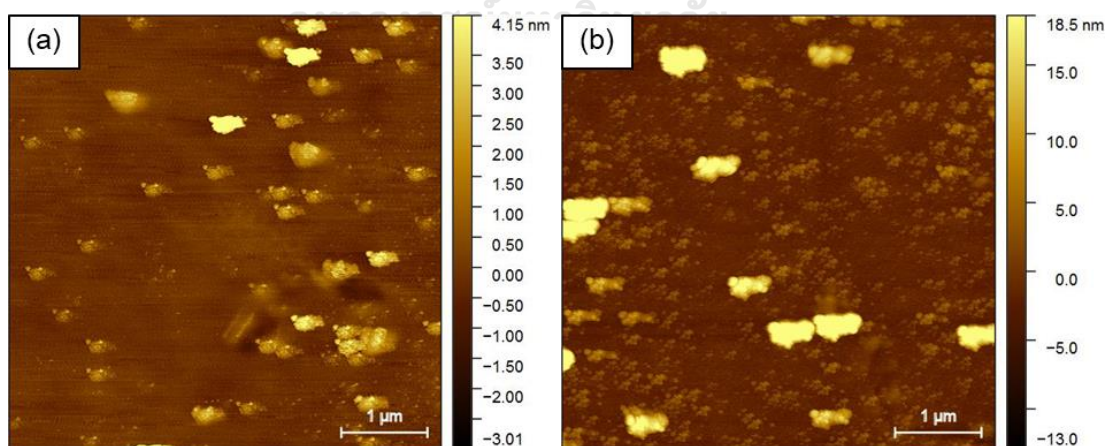


Figure 33 AFM images of 60 W RF sputtering power with (a) 40 nm and (b) 80 nm thickness of SnO₂ films on SLG substrates.

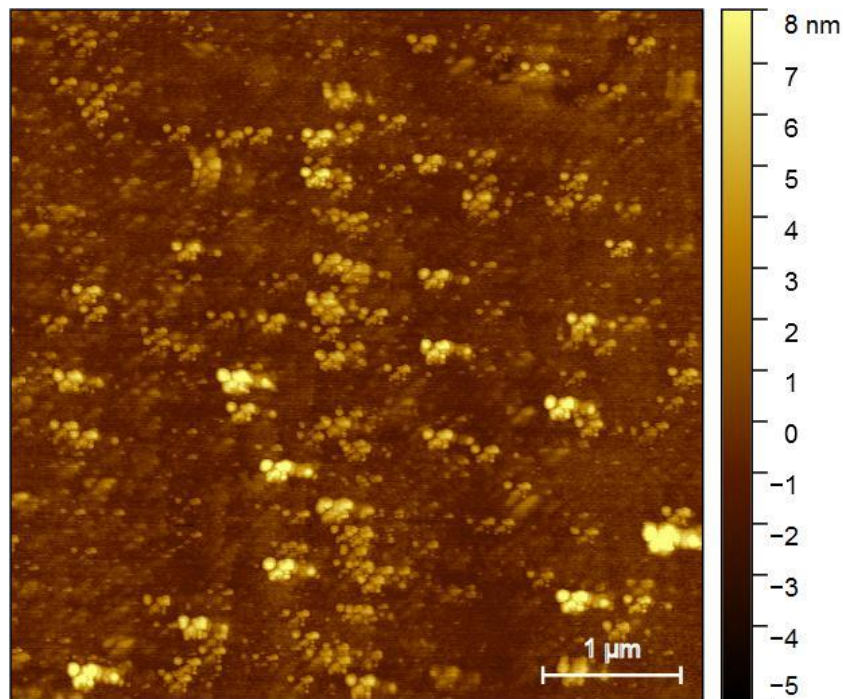


Figure 34 AFM image of 90 W RF sputtering power with 35 nm thickness of SnO₂ films on SLG substrate.

4.2.2 The optical transmission spectrum of sputtered SnO₂ films

The optical transmission of the sputtered SnO₂ films on SLG substrates was greater than 85% in the range from 400 nm to 1100 nm as shown in Figure 35. The high transmission in the visible region (380 – 780 nm) offers a better photon passing to the perovskite absorber. The SnO₂ film deposited by RF sputtering techniques was found to have the band gap energy (E_g) about 4.2 eV.

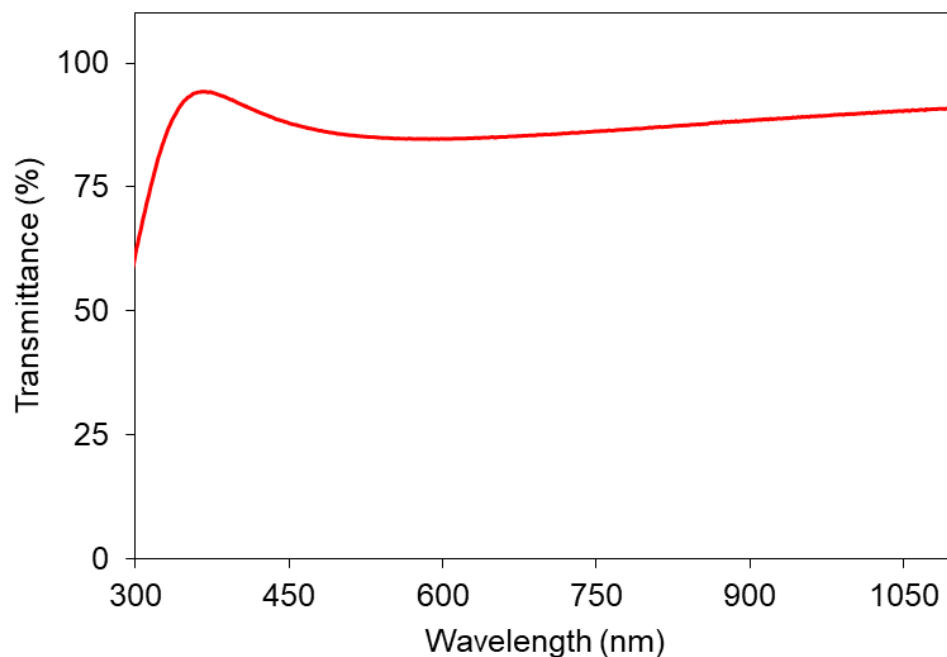


Figure 35 Optical transmission spectrum of the sputtered SnO₂ film on SLG substrates.

4.3 Properties of perovskite solar cells (PSCs)

4.3.1 Characteristics of perovskite absorber layers

Figure 36 shows the perovskite absorber deposited on FTO substrates by the two-step spin-coating method. It can be seen that the perovskite crystals are quite uniform. The shape of perovskite crystal is cuboid, with grain size of approximately 100 nm. The FESEM cross-section image (Figure 37) shows that the thickness of perovskite absorber was about 400 nm. The optical transmission of MAPbI₃ perovskite layers on FTO substrates is shown in Figure 38. The band gap energy (E_g) of perovskite absorber was calculated using the Tauc equation (9):

$$\alpha hv = A(hv - E_g)^{\frac{1}{2}}$$

where A is constant, and hv is the photon energy. The value of E_g was obtained from the plot between $(\alpha hv)^2$ and hv and extrapolation from linear section of the curve to zero on the photon energy axis as shown in Figure 39. For the calculation, the optical band gap of perovskite absorber was about 1.6 eV.

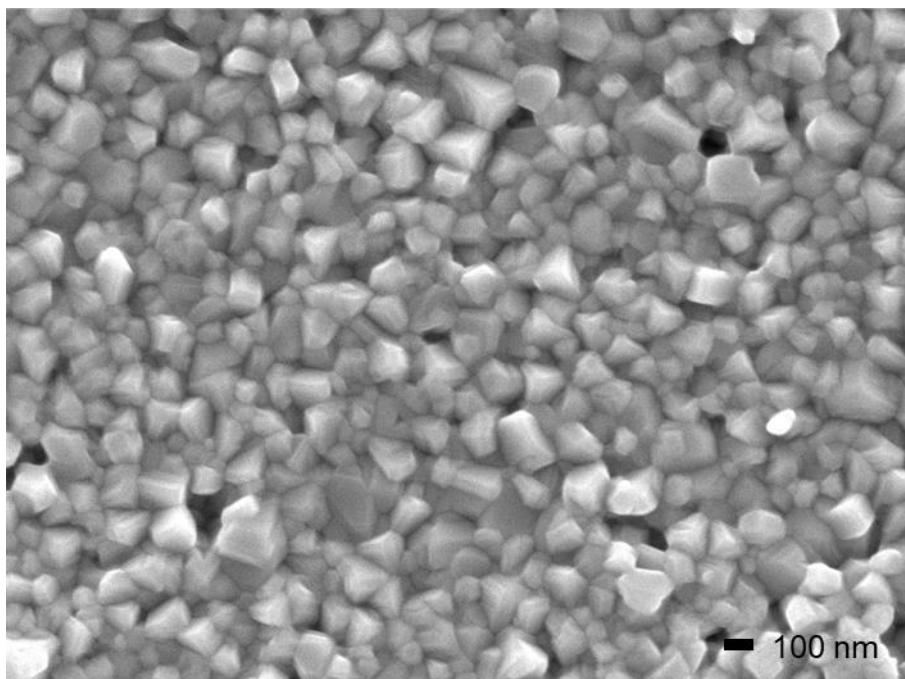


Figure 36 FESEM image of surface morphology of perovskite absorber layers by two-step spin-coating method.

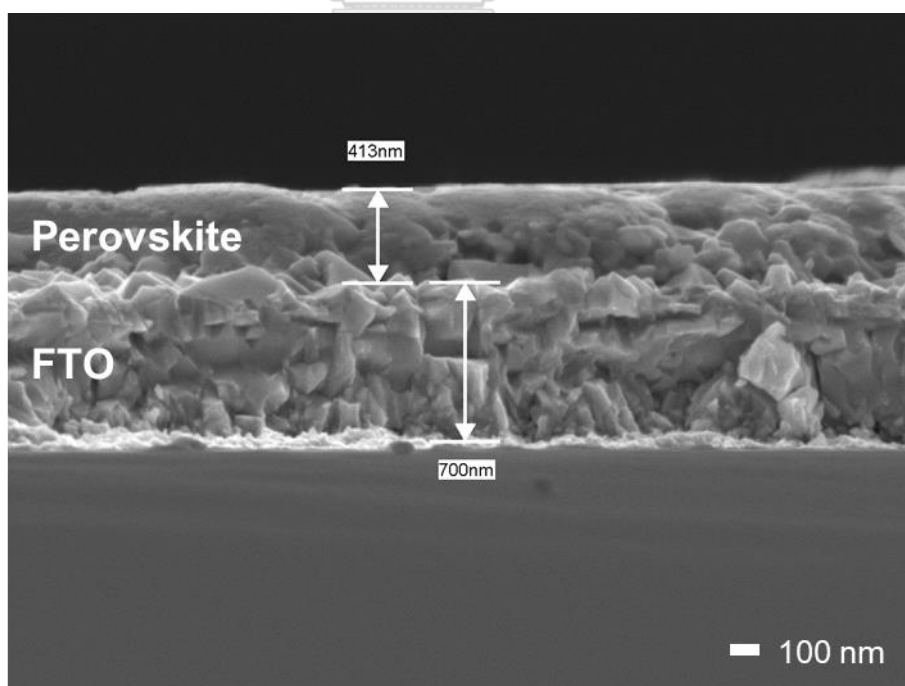


Figure 37 FESEM image of cross-section of perovskite absorber layers on FTO substrates.

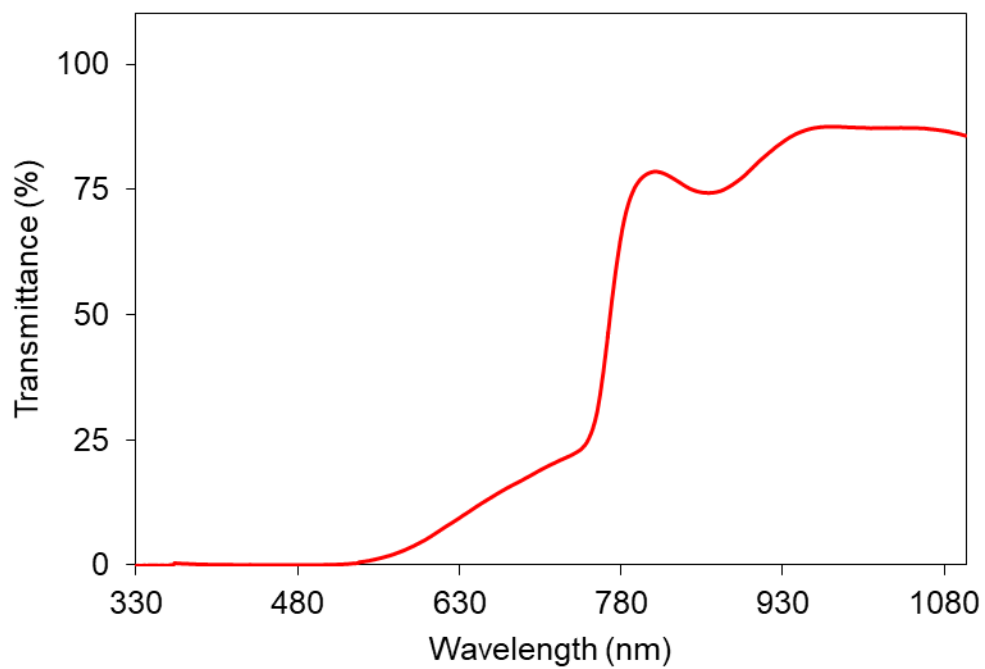


Figure 38 Optical transmission spectrum of perovskite absorber layers by two-step spin-coating method.

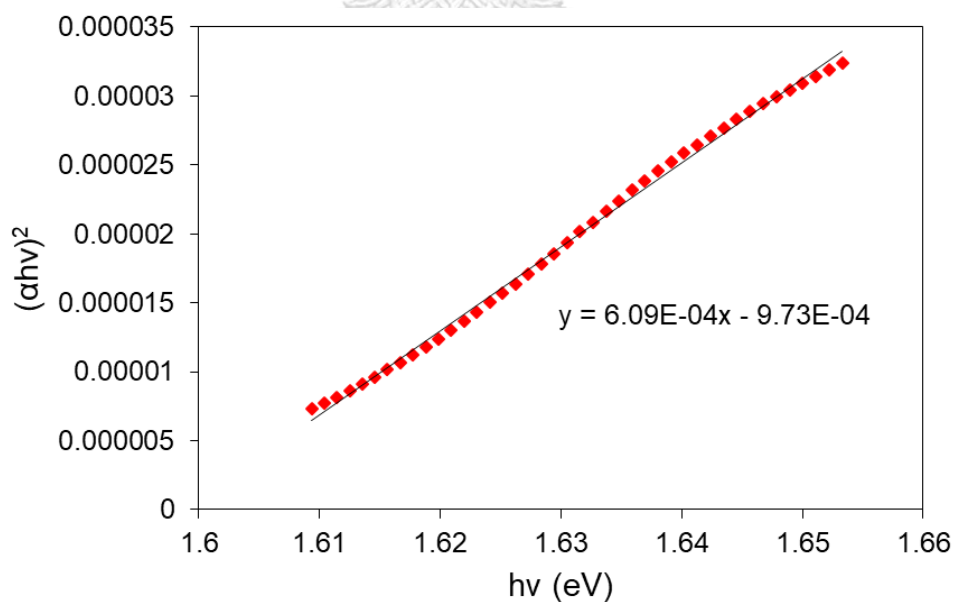


Figure 39 Tauc plot of perovskite absorber layers by two-step spin-coating method.

4.3.2 J-V characteristics of spin-coated SnO₂ films as ETLs

Figure 40 illustrates the cross-section FESEM image of a complete PSCs using the spin-coated SnO₂ films. It can be seen that the device consists of 700 nm of FTO layer, 60 nm of SnO₂ layer, 400 nm of perovskite absorber layer, 100 nm of Spiro-OMeTAD layer, and 120 nm of Au metal electrode layer.

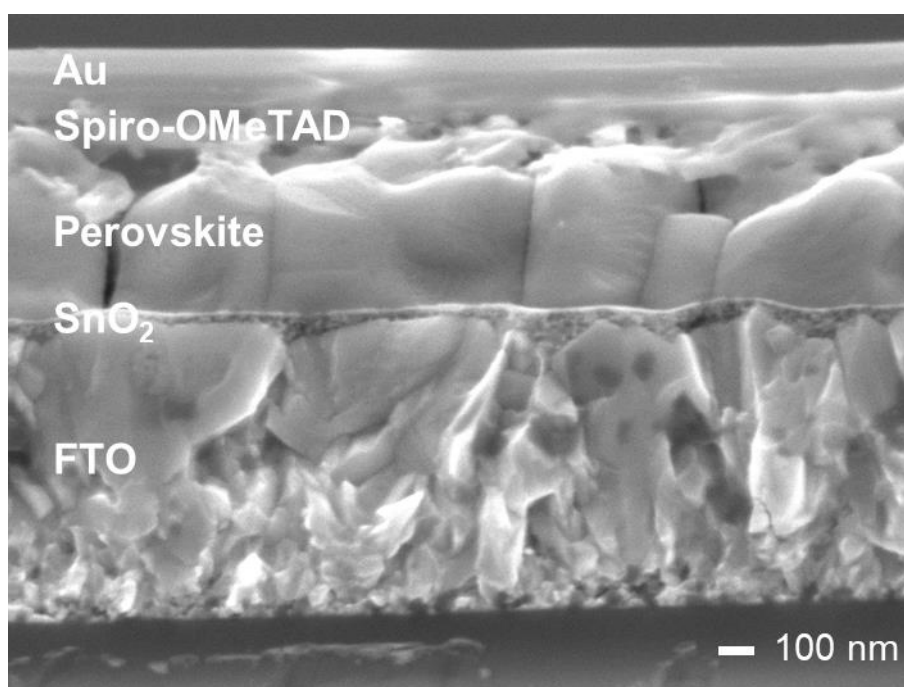


Figure 40 FESEM image of cross-section of a complete PSCs with SnO₂ by spin-coating method.

จุฬาลงกรณ์มหาวิทยาลัย
CHULALONGKORN UNIVERSITY

In this study, the thickness of SnO₂ films by spin-coating was considered by varying spin speed. The thickness increases as the spin speed decreases, and vice versa. The J-V curves of PSCs by spin-coating of SnO₂ were compared by varying spin speed from 2000 rpm to 5000 rpm (Figure 41). The results show that the cell performance decreases as the spin speed increases. The thin SnO₂ films promoted the direct contact between FTO and perovskite absorber and caused the J_{sc} and FF to be reduced. In addition, Figure 42 shows the J-V curves of PSC based on spin-coated SnO₂ films with different precursor concentration using SnCl₄·5H₂O dissolved in IPA (0.1, 0.15, 0.2, 0.25, and 0.5 M), which fixed spin speed (3000 rpm) and annealing temperature. The thickness increases as the precursor concentration increases. The device performance

decreases as the precursor concentration increases that the fill factor was decreased as a result of the thick SnO₂ coatings affecting the high series resistance (R_{series}). The best performance for spin-coated SnO₂ films was obtained from 60 nm thick SnO₂, using spin speed at 3000 rpm for 40 s, and 0.15 M SnCl₄.5H₂O dissolved in IPA. The best device achieved PCE of 12.9% with V_{oc} of 1.04 V, J_{sc} of 18.4 mA/cm², and fill factor of 0.63. Table 5 summarizes the photovoltaic parameters of PSCs based on spin-coated SnO₂ films as ETLs with different spin speed and precursor concentration.

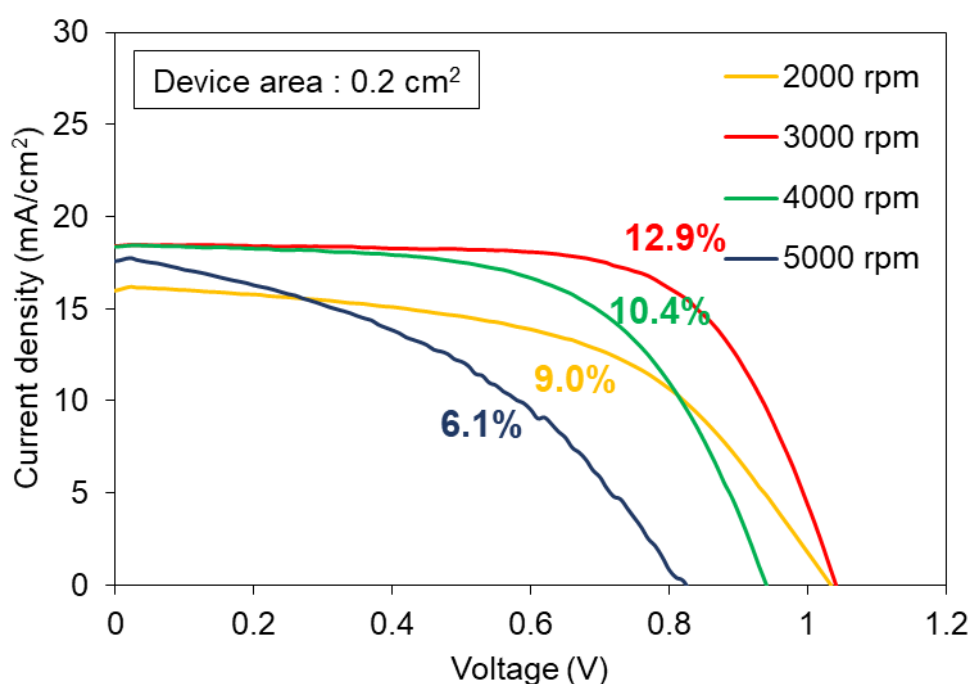


Figure 41 J-V curves of PSCs based on spin-coated SnO₂ films with different spin speed; SnCl₄.5H₂O dissolved in IPA (0.15 M), annealing temperature at 200 °C for 60 min in air.

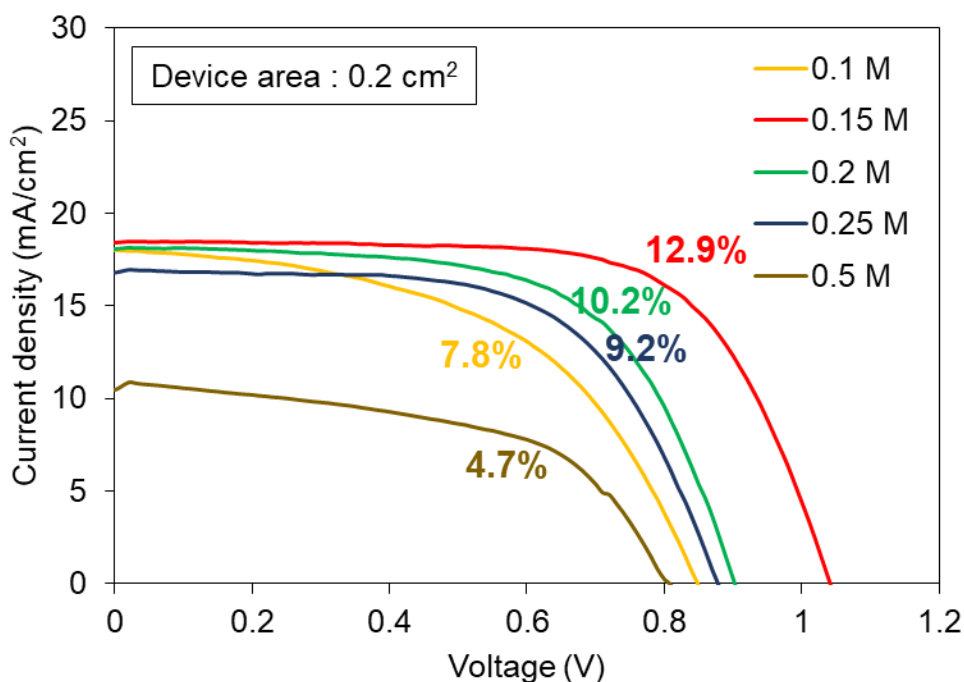


Figure 42 J-V curves of PSCs based on spin-coated SnO_2 films with different $\text{SnCl}_4 \cdot 5\text{H}_2\text{O}$ solution concentration; $\text{SnCl}_4 \cdot 5\text{H}_2\text{O}$ dissolved in IPA, spin speed of 3000 rpm for 40 s, and annealing temperature at 200°C for 60 min in air.

Table 5 Photovoltaic parameters of PSCs with spin-coated SnO_2 films as ETLs with different spin speed and $\text{SnCl}_4 \cdot 5\text{H}_2\text{O}$ solution concentration.

Substrate	V_{oc} (V)	J_{sc} (mA/cm^2)	FF	PCE (%)
Spin speed/time				
2000 rpm/40 s	1.03	16.0	0.54	9.0
3000 rpm/40 s	1.04	18.4	0.68	12.9
4000 rpm/40 s	0.94	18.4	0.60	10.4
5000 rpm/40 s	0.82	17.6	0.42	6.1
Concentration				
0.1 M	0.85	18.0	0.51	7.8
0.15 M	1.04	18.4	0.68	12.9
0.2 M	0.90	18.1	0.62	10.2
0.25 M	0.88	16.8	0.62	9.2
0.5 M	0.81	10.5	0.55	4.7

4.3.3 J-V characteristics of sputtered SnO₂ films as ETLs

In this work, the normal planar structure of PSCs was fabricated using sputtered SnO₂ films as ETLs (Figure 43). Figure 44 shows the cross-section FESEM image of a complete PSC using the sputtered SnO₂ films. It can be seen that the device consists of about 700 nm of FTO layer, 35 - 40 nm of SnO₂ layer, 400 nm of perovskite absorber layer, 100 nm of Spiro-OMeTAD layer, and 120 nm of Au metal electrode layer.

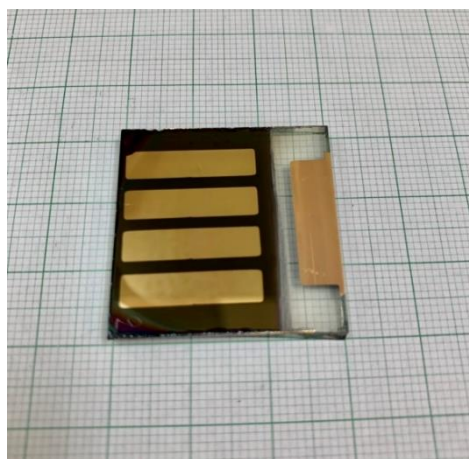


Figure 43 Photograph of a complete PSCs with SnO₂ by RF sputtering techniques.

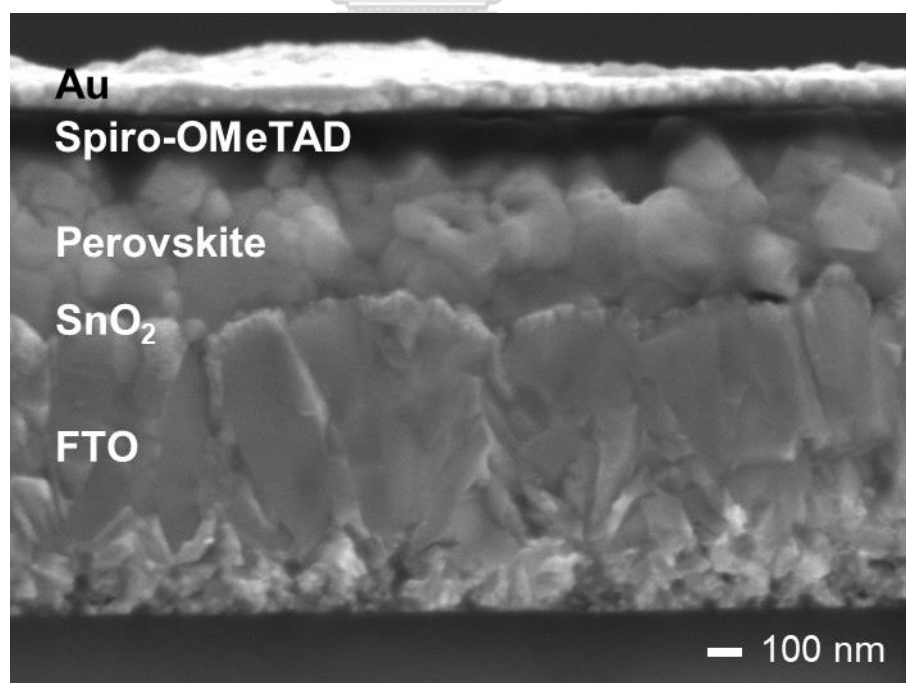


Figure 44 FESEM image of cross-section of a complete PSCs with SnO₂ by RF sputtering techniques.

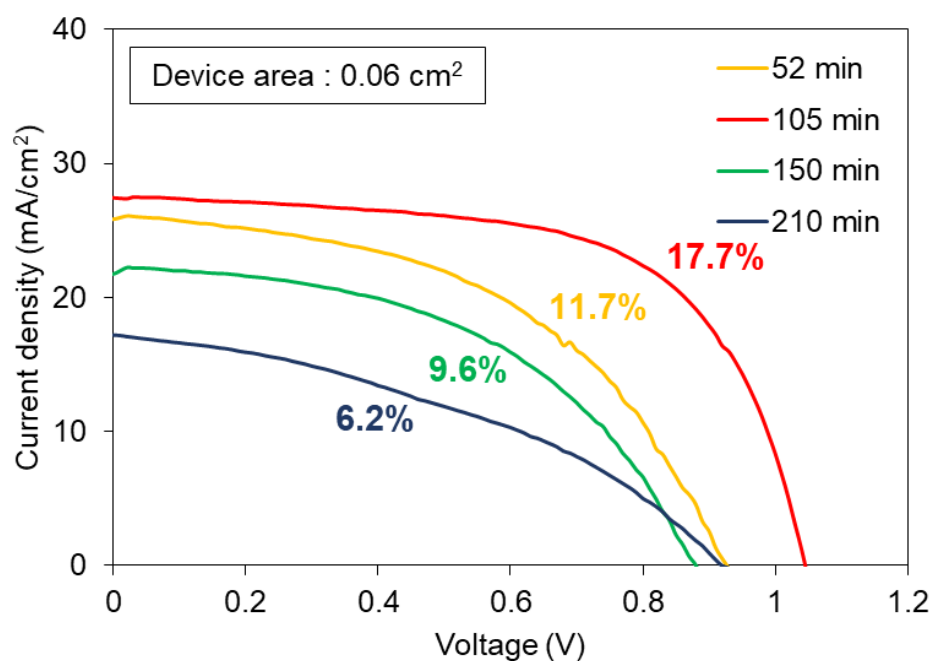
The thicknesses of SnO₂ films with different deposition time were measured by Dektak³ST surface profiler as shown in Table 6. Figure 45 shows the J-V curves of the sputtered SnO₂ films with different deposition time from 52 min to 210 min. In this work, it can be seen that the best device was obtained from 35 - 40 nm thick SnO₂ with deposition time of 105 min with champion PCE of 17.7%, V_{oc} of 1.03 V, J_{sc} of 27.4 mA/cm², and fill factor of 0.63. The thin SnO₂ films could not prevent the carrier recombination at interface of FTO and perovskite absorber.

The J-V curves of the sputtered SnO₂ films were compared with different sputtering power (50, 60, 90, 120, and 150 W). It was shown in the J-V curves in Figure 46 that the performance of PSCs become worsen with increasing RF sputtering power. The main reason is that the sputtering power affects the film density that the inhomogeneous SnO₂ layer exhibited the recombination at SnO₂ and perovskite absorber interface and caused the fill factor to be reduced.

In order to investigate the effect of Ar sputtering gas pressure on the device performance. The complete devices were fabricated on the sputtered SnO₂ films under various Ar gas pressure (1×10^{-3} , 3×10^{-3} , and 6×10^{-3} mbar) while keeping O₂ gas pressure at 1.5×10^{-4} mbar. As shown in figure 47, with decreasing the Ar gas pressure, the device performance was gradually improved. The best device was obtained when the RF sputtering power was 60 W and the Ar gas pressure was 1×10^{-3} mbar, showing high V_{oc} of 1.03 V, J_{sc} of 27.4 mA/cm², fill factor of 0.63, and PCE of 17.7%. The increase in Ar gas pressure results in the decrease of mean free path, leading to the increase in the deposition time to achieve the optimum thickness about 35 - 40 nm. In addition, decreasing the thickness of SnO₂ layer corresponded to increasing of sheet resistance. The detailed photovoltaics parameters of PSCs based on sputtered SnO₂ films as ETLs were listed in Table 7.

Table 6 The thicknesses of SnO₂ films with different deposition time.

Deposition time (min)	Approximate thickness (nm)
52	21 - 30
105	35 - 40
150	47 - 55
210	70 - 98

**Figure 45** J-V curves of PSCs based on sputtered SnO₂ film with different deposition time; RF sputtering power of 60 W and Ar gas pressure of 1×10^{-3} mbar with O₂ gas partial pressure of 1.5×10^{-4} mbar.

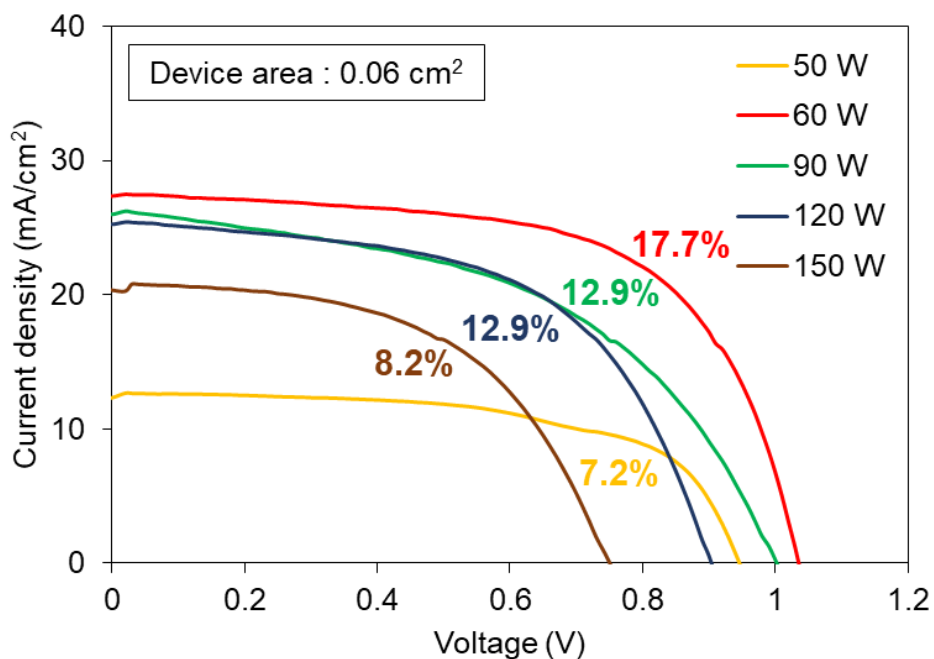


Figure 46 J-V curves of PSCs based on sputtered SnO₂ film with different RF sputtering power; Ar gas pressure of 1×10^{-3} mbar with O₂ gas partial pressure of 1.5×10^{-4} mbar.

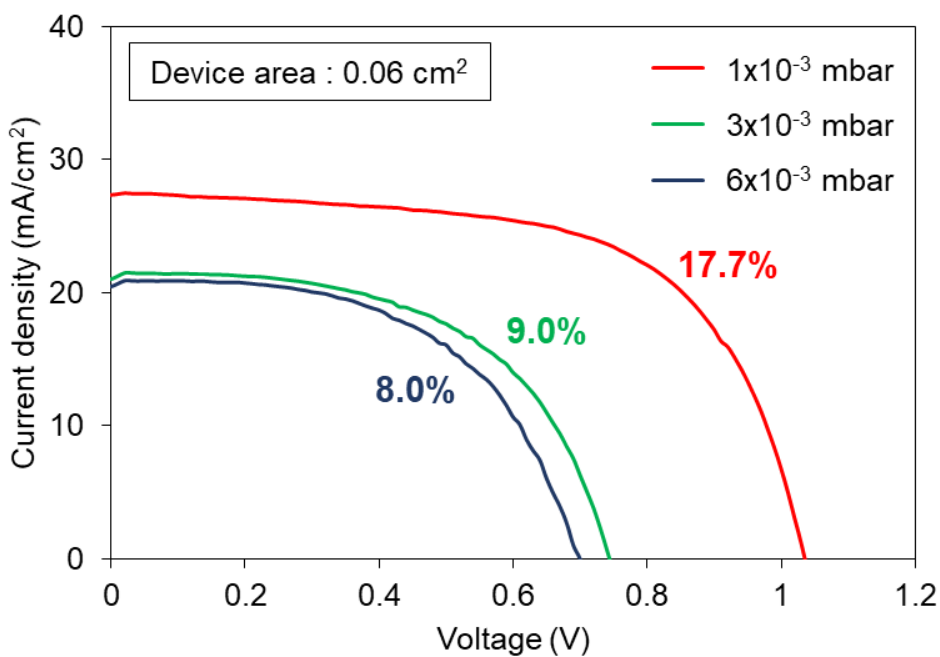


Figure 47 J-V curves of PSCs based on sputtered SnO₂ film with different Ar gas pressures; RF sputtering power of 60 W and O₂ gas partial pressure of 1.5×10^{-4} mbar.

Table 7 Photovoltaic parameters of PSCs with sputtered SnO₂ films as ETLs.

Substrate	V _{oc} (V)	J _{sc} (mA/cm ²)	FF	PCE (%)
Deposition time				
52 min	0.93	25.8	0.49	11.7
105 min	1.03	27.4	0.63	17.7
150 min	0.88	21.7	0.50	9.6
210 min	0.92	17.2	0.39	6.2
RF sputtering power				
50 W	0.95	12.3	0.62	7.2
60 W	1.03	27.4	0.63	17.7
90 W	1.00	26.0	0.50	12.9
120 W	0.90	25.2	0.57	12.9
150 W	0.74	20.3	0.55	8.2
Ar gas pressures				
1 × 10 ⁻³ mbar	1.03	27.4	0.63	17.7
3 × 10 ⁻³ mbar	0.74	21.0	0.58	9.0
6 × 10 ⁻³ mbar	0.70	20.5	0.56	8.0

4.3.4 J-V characteristics of TiO₂ films as ETLs

For comparison, the normal mesoporous structure of PSC was fabricated using spin-coated cp-TiO₂ and mp-TiO₂ as ETLs. The device consists of about 700 nm of FTO layer, 50 nm of cp-TiO₂ layer, 300 nm of mp-TiO₂ layer, 400 nm of perovskite absorber layer, 100 nm of Spiro-OMeTAD layer, and 120 nm of Au metal electrode layer. The J-V curves of the champion PSCs based on spin-coated cp-TiO₂/ mp-TiO₂ and sputtered SnO₂ are both shown in Figure 48. The results show that the device using compact and mesoporous TiO₂ layers as ETLs achieved a PCE higher than 19.0%, a V_{oc} of 1.07 V, a J_{sc} of 25.3 mA/cm², and a fill factor of 0.70. In comparison, the results show that the sputtered SnO₂ as ETL achieved a lower PCE of 17.7%, a V_{oc} of 1.03 V, a J_{sc} of 27.4 mA/cm², and fill factor of 0.63. Moreover, the spin-coated cp-TiO₂/ mp-TiO₂ layers exhibited low series resistance (R_{series}) and high shunt resistance (R_{shunt}).

Table 8 summarizes the photovoltaic parameters of PSCs based on spin-coated cp-TiO₂/ mp-TiO₂ and sputtered SnO₂ layers as ETLs.

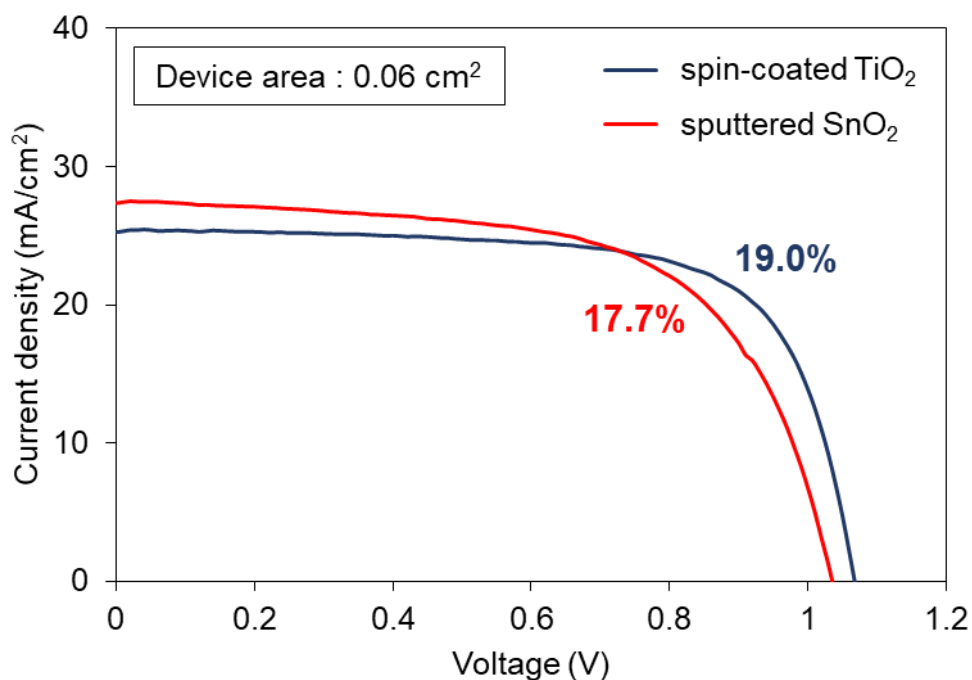


Figure 48 J-V curves of the champion devices based on spin-coated cp-TiO₂/ mp-TiO₂ and sputtered SnO₂ films of PSCs.

Table 8 Photovoltaic parameters of the champion PSCs based on spin-coated cp-TiO₂/ mp-TiO₂ and sputtered SnO₂ films.

Device structure	V _{oc} (V)	J _{sc} (mA/cm ²)	FF	PCE (%)	R _{series} (Ω/cm ²)	R _{shunt} (Ω/cm ²)
Spin-coated cp-TiO ₂ / mp-TiO ₂	1.07	25.3	0.70	19.0	2.06	554.2
Sputtered SnO ₂	1.03	27.4	0.63	17.7	2.49	281.0

CHAPTER V

CONCLUSTION

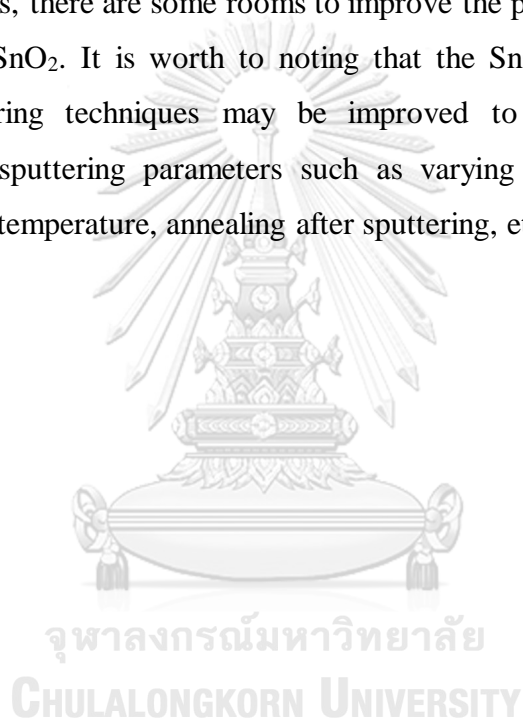
This research presents the physical properties of SnO₂ as ETL prepared by spin-coating and RF magnetron sputtering process and their effects on the performance of planar perovskite solar cells (PSCs)

The fabrication of SnO₂ film by spin-coating method utilized SnCl₄.5H₂O and SnCl₂.2H₂O precursors. The morphology of the spin-coated SnO₂ shows some particulates from recrystallization of SnO₂ precursor on SLG substrates as investigated by FESEM. This results affect the uniformity of the films. The decent SnCl₄.5H₂O precursor concentrations were 0.15 M with the spin speed of 3000 rpm for 40 s and annealing temperature at 200 °C for 60 min in air. This gave a thickness of SnO₂ layer of approximately 60 nm. The best device achieved PCE of 12.9%, V_{oc} of 1.04 V, J_{sc} of 18.4 mA/cm², and fill factor of 0.68. However, wet chemical processes were avoided to minimize the particulates from recrystallization of SnO₂ precursor. This also leads to uneven surface of the ETL layer.

The results suggested that the sputtered SnO₂ films showed very smooth surface as investigated by FESEM. The smoother surface should be beneficial to the light transmission and device performance. AFM images of SnO₂ films fabricated with 90 W sputtering power showed more uniform grains on SLG substrates. This results in the increase of the surface area leading to the increase of photo-generated currents in PSCs. The best condition was obtained when the RF sputtering power was 60 W and the Ar gas pressure was 1×10^{-3} mbar with O₂ gas partial pressure of 1.5×10^{-4} mbar. This gave the optical transmission of SnO₂ layer of approximately 85 - 90% in the visible region. It was found that the device delivered V_{oc} of 1.03 V, J_{sc} of 27.4 mA/cm², fill factor of 0.63, and PCE of 17.7%. The band gap energy (E_g) of SnO₂ was approximately 4.2 eV. The optimum thickness of SnO₂ layer was 35 - 40 nm. The thickness of ETL can affect the device performance essentially. If the ETL is too thick, the device will have too high series resistance, which will reduce the J_{sc} and FF of the device. If the ETL is too thin, there is a more likely of direct contact between FTO and perovskite absorber, which will can cause more carrier recombination.

Lastly, the PSCs in this work were fabricated and compared for the performance of PSCs using SnO₂ and TiO₂ as ETLs. It was found that spin-coated cp-TiO₂ and mp-TiO₂ based devices for mesoporous PSCs were demonstrated to have slightly better device performance than sputtered SnO₂ based devices for planar PSCs. However, TiO₂ has some limitations for PSCs, such as it needs high temperature process, yields low electron mobility, and sensitive to UV illumination. Therefore, SnO₂ is easy preparation at low temperatures and is more stable under UV light than TiO₂.

Despite the fact that the sputtered SnO₂ based devices outperformed spin-coated SnO₂ based devices, there are some rooms to improve the performance of PSCs based on the sputtered SnO₂. It is worth to noting that the SnO₂ films fabricated by RF magnetron sputtering techniques may be improved to achieve higher PCE by optimizing other sputtering parameters such as varying O₂ partial pressure ratio (O₂:Ar), substrate temperature, annealing after sputtering, etc.



REFERENCES

1. Ramanujam, J. and U.P. Singh, *Copper indium gallium selenide based solar cells – a review*. Energy & Environmental Science, 2017. **10**(6): p. 1306-1319.
2. Enam, F.M.T., et al., *Design prospects of cadmium telluride/silicon (CdTe/Si) tandem solar cells from numerical simulation*. Optik, 2017. **139**: p. 397-406.
3. Meng, L., et al., *Improving the efficiency of silicon solar cells using in situ fabricated perovskite quantum dots as luminescence downshifting materials*. Nanophotonics, 2019. **9**(1): p. 93-100.
4. Gong, J., J. Liang, and K. Sumathy, *Review on dye-sensitized solar cells (DSSCs): Fundamental concepts and novel materials*. Renewable and Sustainable Energy Reviews, 2012. **16**(8): p. 5848-5860.
5. Wang, W., et al., *Cosensitized Quantum Dot Solar Cells with Conversion Efficiency over 12*. Adv Mater, 2018. **30**(11).
6. Ratcliff, E.L., B. Zacher, and N.R. Armstrong, *Selective Interlayers and Contacts in Organic Photovoltaic Cells*. J Phys Chem Lett, 2011. **2**(11): p. 1337-50.
7. Correa Baena, J.P., et al., *Highly efficient planar perovskite solar cells through band alignment engineering*. Energy & Environmental Science, 2015. **8**(10): p. 2928-2934.
8. Chen, Y., et al., *Large-area perovskite solar cells – a review of recent progress and issues*. RSC Advances, 2018. **8**(19): p. 10489-10508.
9. Shaikh, J.S., et al., *Nanoarchitectures in dye-sensitized solar cells: metal oxides, oxide perovskites and carbon-based materials*. Nanoscale, 2018. **10**(11): p. 4987-5034.
10. Chang, D.W., et al., *Graphene in photovoltaic applications: organic photovoltaic cells (OPVs) and dye-sensitized solar cells (DSSCs)*. Journal of Materials Chemistry A, 2014. **2**(31).
11. Singh, A.K., et al., *Performance optimization of lead free-MA₂SnI₃ based solar cell with 27% efficiency by numerical simulation*. Optical Materials, 2021. **117**.
12. Boix, P.P., et al., *Current progress and future perspectives for organic/inorganic perovskite solar cells*. Materials Today, 2014. **17**(1): p. 16-23.

13. Lee, J.-W. and N.-G. Park, *Two-step deposition method for high-efficiency perovskite solar cells*. MRS Bulletin, 2015. **40**(8): p. 654-659.
14. Hou, Y., et al., *Enhancement of photovoltaic performance of perovskite solar cells by modification of the interface between the perovskite and mesoporous TiO₂ film*. Solar Energy Materials and Solar Cells, 2016. **155**: p. 101-107.
15. Kim, H.S. and N.G. Park, *Parameters Affecting I-V Hysteresis of CH₃NH₃PbI₃ Perovskite Solar Cells: Effects of Perovskite Crystal Size and Mesoporous TiO₂ Layer*. J Phys Chem Lett, 2014. **5**(17): p. 2927-34.
16. Liu, D., J. Yang, and T.L. Kelly, *Compact layer free perovskite solar cells with 13.5% efficiency*. J Am Chem Soc, 2014. **136**(49): p. 17116-22.
17. Yi, H., et al., *Bilayer SnO₂ as Electron Transport Layer for Highly Efficient Perovskite Solar Cells*. ACS Applied Energy Materials, 2018. **1**(11): p. 6027-6039.
18. Ganchev, M., et al., *Spin – coating of SnO₂ thin films*. Journal of Physics: Conference Series, 2019. **1186**.
19. Qiu, L., et al., *Scalable Fabrication of Stable High Efficiency Perovskite Solar Cells and Modules Utilizing Room Temperature Sputtered SnO₂ Electron Transport Layer*. Advanced Functional Materials, 2018. **29**(47).
20. Meng, X., et al., *Three growth modes and mechanisms for highly structure-tunable SnO₂ nanotube arrays of template-directed atomic layer deposition*. Journal of Materials Chemistry, 2011. **21**(33).
21. Bu, T., et al., *A novel quadruple-cation absorber for universal hysteresis elimination for high efficiency and stable perovskite solar cells*. Energy & Environmental Science, 2017. **10**(12): p. 2509-2515.
22. Jiang, Q., X. Zhang, and J. You, *SnO₂ : A Wonderful Electron Transport Layer for Perovskite Solar Cells*. Small, 2018: p. e1801154.
23. Jung, K.-H., et al., *Solution-processed SnO₂ thin film for a hysteresis-free planar perovskite solar cell with a power conversion efficiency of 19.2%*. Journal of Materials Chemistry A, 2017. **5**(47): p. 24790-24803.

24. Kam, M., et al., *Room-Temperature Sputtered SnO₂ as Robust Electron Transport Layer for Air-Stable and Efficient Perovskite Solar Cells on Rigid and Flexible Substrates*. *Sci Rep*, 2019. **9**(1): p. 6963.
25. Bai, G., et al., *High performance perovskite sub-module with sputtered SnO₂ electron transport layer*. *Solar Energy*, 2019. **183**: p. 306-314.
26. Leng, D., et al., *Preparation and Properties of SnO₂ Film Deposited by Magnetron Sputtering*. *International Journal of Photoenergy*, 2012. **2012**: p. 1-6.
27. Ke, W., et al., *Low-temperature solution-processed tin oxide as an alternative electron transporting layer for efficient perovskite solar cells*. *J Am Chem Soc*, 2015. **137**(21): p. 6730-3.
28. Xiong, L., et al., *Review on the Application of SnO₂ in Perovskite Solar Cells*. *Advanced Functional Materials*, 2018. **28**(35).
29. Shi, Y., et al., *CH₃NH₃PbI₃ and CH₃NH₃PbI₃-xCl_x in Planar or Mesoporous Perovskite Solar Cells: Comprehensive Insight into the Dependence of Performance on Architecture*. *The Journal of Physical Chemistry C*, 2015. **119**(28): p. 15868-15873.
30. Zhou, D., et al., *Perovskite-Based Solar Cells: Materials, Methods, and Future Perspectives*. *Journal of Nanomaterials*, 2018. **2018**: p. 1-15.
31. Li, S., et al., *A brief review of hole transporting materials commonly used in perovskite solar cells*. *Rare Metals*, 2021. **40**(10): p. 2712-2729.
32. Kurdesau, F., et al., *Comparative study of ITO layers deposited by DC and RF magnetron sputtering at room temperature*. *Journal of Non-Crystalline Solids*, 2006. **352**(9-20): p. 1466-1470.
33. Singh, A.K., *Experimental Methodologies for the Characterization of Nanoparticles*, in *Engineered Nanoparticles*. 2016. p. 125-170.
34. Butt, H.-J., B. Cappella, and M. Kappl, *Force measurements with the atomic force microscope: Technique, interpretation and applications*. *Surface Science Reports*, 2005. **59**(1-6): p. 1-152.



จุฬาลงกรณ์มหาวิทยาลัย
CHULALONGKORN UNIVERSITY

VITA

NAME Miss Rattanaphon Thanimkan

DATE OF BIRTH 23 Feb 1995

PLACE OF BIRTH Nakhon Si Thammarat

HOME ADDRESS 36/1 Village No.6 Chalong Sub-district, Sichon District,
Nakhon Si Thammarat, 80120, Thailand

PUBLICATION -

AWARD RECEIVED -



จุฬาลงกรณ์มหาวิทยาลัย
CHULALONGKORN UNIVERSITY